

USC-SIPI REPORT #409

Assessment of Myocardial Blood Flow in Human Using Arterial Spin Labeled MRI

by

Zungho Zun

December 2010

**Signal and Image Processing Institute
UNIVERSITY OF SOUTHERN CALIFORNIA
Viterbi School of Engineering
Department of Electrical Engineering-Systems
3740 McClintock Avenue, Suite 400
Los Angeles, CA 90089-2564 U.S.A.**

ASSESSMENT OF MYOCARDIAL BLOOD FLOW IN HUMANS USING
ARTERIAL SPIN LABELED MRI

by

Zungho Zun

A Dissertation Presented to the
FACULTY OF THE USC GRADUATE SCHOOL
UNIVERSITY OF SOUTHERN CALIFORNIA
In Partial Fulfillment of the
Requirements for the Degree
DOCTOR OF PHILOSOPHY
(ELECTRICAL ENGINEERING)

December 2010

Copyright 2010

Zungho Zun

Acknowledgements

I am grateful for the support of as many people as were the days I spent pursuing this PhD degree.

I am most grateful to my adviser Professor Krishna Nayak and his Magnetic Resonance Engineering Laboratory (MREL). If it was not for him, I would not have had a chance to learn MRI, a field which I now truly enjoy working on and which I feel is the area of study that best suits me. Krishna has also been the best adviser I could possibly have wished for to guide me through my PhD dissertation. I truly learned a lot from him about how to approach research in a science-oriented manner and tackle research problems step by step. Now I am graduating and moving to a new place for the next level of my career, but I will always be proud that I am from his laboratory.

I have also been fortunate to work with Professor Eric Wong at UC San Diego. It has been a great honor to collaborate with someone who is a guru in one topic. He has amazed me with his hard work and noble ideas on research and is a great role model for me to follow. I am also grateful for his time and effort during his multiple visits to USC and our many phone discussions.

I would like to thank Dr. Ramdas Pai and Dr. Padmini Varadarajan for being always supportive of our clinical studies at Loma Linda University Hospital as well as providing invaluable suggestions. I thank Dr. Gerald Pohost for his clinical advice on my project. I thank Dr. Houchun Harry Hu for numerous times of assistance. He has been helpful for almost everything from volunteering to giving advice on my academic path.

I should not forget to express my gratitude to my previous and present labmates at MREL because it always makes me smile when I look back on memories of them. In particular, Dr. Taehoon Shin was a good labmate who not only shared an office with me for many years, but also shared many research/fun activities. I thank Mahender Makhijani, Yoon-Chul Kim, Travis Smith, Samir Sharrma, and all the junior students for being friendly and helpful.

Lastly, my deep gratitude goes to my family for their endless love and support. Mom and Dad were always supportive and on my side from the moment I decided to study in USA. My three sisters have cared about me and have given me strength by believing in me. I am also grateful to my fiancé Eun Kyung, soon-to-be my family. She has brought me spiritual peace during the last part of my PhD years.

Table of Contents

Acknowledgements	ii
List of Tables	vii
List of Figures	viii
Abstract	xii
1 Introduction	1
1.1 Organization of This Dissertation.....	3
2 Background	5
2.1 MRI Physics.....	5
2.1.1 Nuclear Magnetic Resonance.....	5
2.1.2 Excitation.....	8
2.1.3 Relaxation.....	12
2.2 Myocardial Perfusion.....	14
2.2.1 Coronary Artery Disease.....	14
2.2.2 Myocardial Perfusion Imaging.....	16
2.3 Arterial Spin Labeled MRI.....	17
2.3.1 Basic Concepts.....	17
2.3.2 Pre-clinical Applications.....	20
2.4 Myocardial ASL.....	21
2.4.1 Unique Challenges for ASL in the Heart.....	21
2.4.2 Cardiac Physiology.....	22
2.4.3 Myocardial ASL in Animals.....	23
2.4.4 Previous Studies on Myocardial ASL in Humans.....	24
2.4.5 Myocardial ASL at 3 Tesla.....	25
3 Graphical Analysis of Balanced Steady-state Free Precession	27
3.1 Matrix Analysis.....	29
3.2 Graphical Analysis.....	32
3.2.1 On-resonance.....	32
3.2.2 Off-resonance.....	36
3.3 Discussion.....	39

4	Feasibility of Myocardial Arterial Spin Labeling in Humans	42
4.1	Methods	43
4.1.1	Pulse Sequence	43
4.1.2	Reconstruction	45
4.1.3	Quantification	46
4.1.4	Noise Analysis	46
4.1.5	Experimental Methods	49
4.2	Results	50
4.2.1	Resting MBF	50
4.2.2	Dependence on Inflow	54
4.2.3	Modulation with Mild Stress	55
4.3	Discussion	56
5	Measurement of Changes in Myocardial Perfusion with Vasodilatation	62
5.1	Methods	63
5.1.1	Study Design	63
5.1.2	Imaging Methods	65
5.1.3	Data Analysis	66
5.2	Results	67
5.2.1	Normal Subjects	67
5.2.2	Comparison of Normal and Ischemic Segments	69
5.2.3	Subjects with Single-vessel Disease	70
5.3	Discussion	72
6	Attempts to Reduce Physiological Noise	76
6.1	Myocardial Background Suppression	77
6.1.1	Methods	77
6.1.2	Results	78
6.1.3	Discussion	79
6.2	Blood Pool Signal Suppression Using Pulsed 2D Tagging	80
6.2.1	Methods	80
6.2.2	Results	83
6.2.3	Discussion	84
6.3	Breath-hold Duration Reduction Using Pre-saturation	85
6.3.1	Methods and Results	85
6.3.2	Discussion	88

7	Summary and Future Work	89
7.1	Summary	89
7.2	Future Work	90
7.2.1	Extended Spatial Coverage.....	90
7.2.2	Systolic Imaging.....	91
7.2.3	Other Tagging Methods.....	91
7.2.4	Cross-validation with Other Modalities	92
	References	94

List of Tables

4.1. MBF measurements in healthy volunteers at rest. Columns contain the measured MBF, SNR, size of the septal ROI, standard deviation of measured MBF, and confidence (probability of measured MBF error being < 0.1 ml/g/min) from fifteen scans of healthy subjects. Data are sorted in ascending order according to measured MBF.....	52
4.2. MBF measurements (in ml/g/min) with different slab-selective inversion thicknesses (3 cm for slice, 12 cm for LV, and nonselective for everything).....	55
4.3. MBF measurements (in ml/g/min) at rest, with passive leg elevation, and with isometric handgrip exercise, and heart rates (HR, in bpm) for each study. The average heart rate change from rest was -1% with leg elevation and 0.3% with handgrip.....	56
5.1. Comparison of normal myocardial segments from the normal patients and the most ischemic myocardial segments from the patients with angiographically-significant CAD. *The difference in perfusion reserve between normal and ischemic segments was statistically significant ($p=0.0419$), based on Student's unpaired t-test.....	70
6.1. Average myocardial signal on control and tagged images with respect to equilibrium signal, MBF estimate (in ml/g/min), and standard deviation of physiological noise (in ml/g/min).....	79
6.2. Inversion efficiency across the proximal aorta, residual LV signal ((C-T)/C on LV blood), MBF measurements (in ml/g/min), and SD of physiological noise (in ml/g/min) for 1D and 2D tagging schemes.....	84
6.3. MBF measurements and SD of physiological noise using FAIR with $T_{\text{delay}} = 6$ sec and FAIRER with $T_{\text{delay}} = 0$ sec (in ml/g/min).....	87

List of Figures

2.1. Polarization of magnetic spins. Left: Spins are randomly oriented under normal condition. Right: With the external magnetic field B_0 , two effects occur; (1) spins are aligned with the direction of B_0 , (2) spins exhibit resonance around B_0 at a known resonance frequency.	6
2.2. Illustration of magnetization. Magnetization is aligned with B_0 at equilibrium and rotates around B_0 based on left hand rule. When thumb points in the magnetic field direction, the fingers point in the precession direction.	7
2.3. Magnetization excitation viewed in the rotating frame. The direction of rotation caused by B_1 can be found using the same left hand rule as used with B_0	8
2.4. Illustration of 90° excitation and 180° excitation (or inversion). B_1 determines the flip-angle of excitation.	9
2.5. Illustration of adiabatic excitation for 180° flip-angle (inversion). Magnetization is effectively locked to \mathbf{B}_{eff} by rapid rotation around it, and follows the passage of \mathbf{B}_{eff}	11
2.6. Relaxation behavior of longitudinal and transverse components of magnetization in blood and myocardium after 90° excitation. T_1/T_2 of the blood and myocardium are known to be 1512 ms/141 ms and 1115 ms/41 ms at 3T, respectively [7].	13
2.7. Illustration of narrowing of the coronary vessels due to accumulation of plaques within the vessel walls.	15
2.8. Examples of myocardial perfusion imaging with (A) SPECT and (B) PET [41].	17
2.9. Generic diagram for ASL. ASL image is the difference of tagged (image with tagging) and control (image without tagging) images (figure courtesy of Eric Wong).	19

2.10. Illustration of arterial blood magnetization in control and tagged images as a function of time.	20
2.11. Example ASL images from brain (A), lung (B), lower legs (C) (courtesy of Eric Wong), and kidney (D) [25].	21
3.1. Alternating balanced SSFP profiles according to different flip angles for $T_1/T_2=1000\text{ms}/300\text{ms}$. θ denotes off-resonance precession within TR. In the steady state, $M_5=M_1$	28
3.2. RF sequence of alternating balanced SSFP. M_x 's denote the vector magnetization right before or after the excitation. In the steady state, $M_5=M_1$	31
3.3. Steady-state magnetizations of alternating balanced SSFP on resonance with exaggerated relaxation. Symmetry about z-axis requires that the four magnetization vectors have the same magnitude, which means that $(\Delta M_{XY}, \Delta M_Z)$ from relaxation must be perpendicular to the magnetization position vector (M_{XY}, M_Z)	33
3.4. Magnetization (M_{XY}, M_Z) in the steady state as a function of α . When magnetization reaches the rightmost point of the ellipse, the greatest transverse signal is produced.	35
3.5. Balanced SSFP with off-resonance precession in the steady state. Solid and dotted arrows denote precession and instant excitation respectively. a: Magnetizations immediately before and after RF pulse. b: Magnetizations at $TE=TR/2$. The effective flip angle α' is equivalent to the sum of two angles that each magnetization in a forms with z-axis.	37
3.6. Effective flip angle, magnetization at echo time, and steady-state signal as a function of prescribed flip angle and off-resonance θ . For $\alpha=10^\circ$ (top row), $\alpha=40^\circ$ (middle row), and $\alpha=140^\circ$ (bottom row), the figures show how the effective flip angle, $M(TE)$, and transverse component profile are related as off-resonance changes. $T_1=1000\text{ms}$, $T_2=300\text{ms}$, and $TE=TR/2$	38
3.7. Signal profile based on graphical derivation or simulation with approximation (a) and the simulation without approximation (b) for extremely small flip angle. According to the exact simulation, one peak is observed at $\theta=180^\circ$ instead of two peaks.	41

4.1. Myocardial ASL pulse sequence. Tagging and imaging are both centered at mid-diastole. Using Flow-induced Alternating Inversion Recovery (FAIR), preparatory inversion pulses are either slab-selective or non-selective to generate control or tagged images, respectively. Imaging is performed using a snapshot balanced steady-state free precession (SSFP) sequence that is preceded by fat saturation, to reduce signal from epicardial fat, and a 5-tip linear ramp preparation, to minimize transient signal oscillations. During each breath-hold, one control image and one tagged image are acquired with a 6-second pause in between.	44
4.2. Measured resting MBF as a function of the number of voxels averaged. Roughly 80 voxels were segmented for each breath-hold, resulting in a measurement of 0.70 ml/g/min based on 6 breath-holds (right-most data point). All other data points were simulated by considering subsets of the 6 breath-holds.....	53
4.3. Six MBF measurements averaged for each breath-hold with alternating control/tagging image order. The solid line in the middle corresponds to the MBF value averaged over all voxels from six breath-holds (0.70 ml/g/min), and two dotted lines represent estimated upper (0.70+0.24 ml/g/min) and lower (0.70-0.24 ml/g/min) bounds of signal deviation due to incomplete static tissue relaxation.....	54
5.1. Modified stress CMR protocol. Myocardial ASL scans are performed at rest and during adenosine infusion, both prior to first-pass imaging to avoid confounding effects of the contrast agent (lowering the blood T ₁). The CMR protocol after completion of adenosine infusion is unchanged and includes viability and function imaging.	64
5.2. MBF estimates at rest (blue) and during adenosine infusion (purple), in eleven patients with no significant perfusion defect on first-pass imaging, and no significant disease on coronary angiography. The average MBF was 1.09 ± 0.70 ml/g/min at rest and 3.92 ± 1.08 ml/g/min with adenosine, yielding an average perfusion reserve (MBF _{stress} /MBF _{rest}) of 4.29. This increase in MBF was found to be statistically significant based on Student's paired t-test (p=0.00002). Error bars represent plus or minus one standard deviation of the measured physiological noise. The average physiological noise during adenosine infusion was 2.6 times larger than the average physiological noise at rest.	68

5.3. Myocardial ASL perfusion reserve maps and X-ray angiograms from the first two patients with single-vessel CAD. A, B: patient with total LAD occlusion, C, D: patient with total RCA occlusion. Myocardial regions with lowered perfusion reserve are consistent with the territories of occluded vessels (see arrows).	71
5.4. Standard deviation of physiological noise as a function of ROI size, averaged across 19 patients in resting scans. If physiological noise was not spatially correlated at all, the standard deviation should be inversely proportional to the square root of ROI size (as indicated by “Reference”).	74
6.1. Cardiac gated FAIR – SSFP pulse sequences A: without and B: with myocardial BGS.	78
6.2. 2D selective adiabatic inversion pulse. (23 ms duration, 0.16 G peak B_1+).	82
6.3. Cardiac gated “pulsed” myocardial ASL sequence.	82
6.4. In-vivo tag profiles for A: 1D tagging and B: 2D tagging of the proximal aorta. Identically windowed difference images for C: 1D tagging and D: 2D tagging.	83
6.5. Myocardial ASL pulse sequence of FAIR or FAIRER in each breath-hold. Control and tagged imaging are separated by T_{delay}	86
6.6. MBF error due to imperfect static tissue subtraction as a function of time delay between control and tagged imaging.	87

Abstract

Magnetic resonance imaging (MRI) is a powerful imaging modality that is both non-invasive and non-ionizing. MRI can be used to facilitate the evaluation of coronary artery disease (CAD), which is a leading cause of death worldwide. In particular, MRI-based first-pass techniques provide assessment of myocardial perfusion with high resolution in detection of CAD. Myocardial perfusion reflects the rate of blood delivery to tissue and is a powerful indicator of tissue health. However, these first-pass methods require the use of contrast agent which cannot be applied to the patients with end-stage renal disease (ESRD). This dissertation contributes a new method for measuring myocardial perfusion without contrast agent, using arterial spin labeled (ASL) MRI.

Firstly, a graphical analysis of balanced steady-state free precession (SSFP) is presented. Balanced SSFP is an imaging sequence that provides high signal-to-noise ratio (SNR) efficiency. Because ASL-based perfusion imaging typically suffers from low intrinsic SNR, balanced SSFP was adopted as our proposed imaging sequence though this dissertation. The graphical approach provides an intuition for understanding balanced SSFP.

Secondly, the feasibility of myocardial perfusion imaging using ASL (or myocardial ASL) is demonstrated in healthy volunteers. It is shown that myocardial ASL measurements are consistent with previous published literature values of perfusion using positron emission tomography (PET), are inflow-dependent, and increase with mild stress. In addition, analysis of noise is presented to assess its impact on ASL measurement error.

Thirdly, the potential of myocardial ASL to detect angiographically significant CAD is demonstrated in patients. The perfusion reserve index is defined as the rate of perfusion during stress divided by that at rest. It is a measure of the severity of CAD. This study performed rest-stress myocardial ASL scans using vasodilator in patients with suspected CAD. Measured perfusion in normal myocardial segments increased by a factor of four during stress, matching literature values based on PET. There was also a statistically significant difference in perfusion reserve between normal and the most ischemic myocardial segments, which suggests that myocardial ASL may be capable of detecting CAD.

Lastly, three attempts to improve measurement confidence in myocardial ASL are described. Three potential sources of measurement noise are identified and a relevant solution to each noise source is presented. Physiological noise is measured with and without the solution and statically significant reduction is examined.

Chapter 1

Introduction

Magnetic resonance imaging (MRI) is a powerful imaging modality because it is non-invasive and utilizes no ionizing radiation. MRI provides structural imaging with excellent soft tissue contrast and high spatial resolution. It can also provide functional measurements such as blood flow, blood oxygenation, diffusion of water molecules, and chemical composition.

Coronary artery disease (CAD) is a leading cause in the world. In USA alone, half a million people die due to CAD annually. Additionally, more than 10 million single-photon emission computed tomography (SPECT) scans are performed for myocardial perfusion imaging (MPI) each year. In the diagnosis of CAD, MPI plays an important role by measuring blood flow in heart muscle (myocardium). MPI is typically performed using SPECT or positron emission tomography (PET); however they are both expensive, involve exposure to ionizing radiation, and provide low spatial resolution. MRI-based first-pass methods allow for MPI without radiation and with high spatial resolution. While these techniques are promising and becoming widely-used,

they require the use of contrast agents. This limits the repeated or real-time scanning, and more importantly, it is not applicable to patients with renal failure.

Arterial spin labeling (ASL) is an MRI-based method that can quantitatively measure tissue blood flow without contrast agent. ASL applied to myocardial perfusion has several potential advantages over contrast-based MPI methods. First, the ASL signal is directly proportional to tissue blood flow, and therefore quantitation of myocardial blood flow (MBF) should come more naturally. This has the potential to reduce the problem of inter-observer variability that affects qualitative first-pass MR perfusion imaging. Second, ASL does not require any contrast agents, resulting in reduced cost and reduced side effects. Third, ASL can be performed continuously, which could open up new opportunities for repeated or even real-time monitoring of patients (e.g. before, during, and after interventions). Finally, ASL has a potential for the mapping of vascular territories in myocardium, allowing for evaluation of potential vascular blockage and stenoses.

The overall aim of this work is to validate myocardial ASL in humans with our proposed sequence, and demonstrate its potential to detect angiographically significant CAD.

1.1 Organization of This Dissertation

The remainder of this dissertation is organized as follows

Chapter 2: Background

This chapter contains an overview of MR physics, basic concepts of myocardial perfusion imaging, and the generic mechanism of ASL perfusion imaging. The application of ASL to myocardial perfusion imaging is described with its unique challenges.

Chapter 3: Graphical Analysis of Balanced Steady-state Free Precession

SSFP is an imaging method that provides very high signal-to-noise ratio (SNR) efficiency, and is used in our work. This chapter presents a novel graphical approach to the solution of the steady-state magnetization in balanced SSFP for intuitive understanding. The solution of magnetization derived using Bloch equation is provided and compared with graphical derivation [105].

Chapter 4: Feasibility of Myocardial Arterial Spin Labeling in Humans

This chapter describes the development of myocardial ASL using FAIR tagging and SSFP imaging, and our initial demonstration of feasibility in healthy volunteers. This study also presents an analysis of thermal and physiological noise [108, 109].

Chapter 5: Measurement of Changes in Myocardial Perfusion with Vasodilatation

This chapter describes application of the proposed myocardial ASL method in suspected patients, and demonstrates the clinically relevant increase in MBF measurements with vasodilatation. MBF measurements in patients with and without CAD confirm a potential of myocardial ASL to diagnose myocardial ischemia [112-114].

Chapter 6: Methods for Reducing Physiological Noise

We found that physiological noise is primarily responsible for the limited sensitivity of myocardial ASL. This chapter describes three different approaches to reduce physiological noise using background suppression, blood pool signal suppression, and shorter breath-holds [106, 107, 110, 111].

Chapter 7: Summary and Future Work

This chapter summarizes this dissertation and suggests several areas for future work.

Chapter 2

Background

2.1 MRI Physics

2.1.1 Nuclear Magnetic Resonance

In 1946, Felix Bloch theorized any spinning charged nucleus creates an electromagnetic field [8]. The magnetic component of this field causes atoms with an odd number of protons and/or of neutrons to possess a nuclear spin angular momentum or simply spin. These spins can be visualized as spinning charged spheres, and act like tiny bar magnets.

In the absence of an external magnetic field, the spins are randomly oriented and the net magnetic field of spin ensemble is zero. With an external magnetic field B_0 , however, these spins have two properties. First, the direction of magnetic field in each spin is all aligned with the direction of B_0 , yielding a nonzero net magnetic moment. Roughly half of spins are parallel to the direction of B_0 and, the other half are anti-parallel to the direction of B_0 . There are slightly more

spins that are parallel, and this difference (7 in 2×10^6 for hydrogen at 1.5 T) is utilized in MR imaging. Second, these spins are all rotating around the direction of B_0 at a resonance frequency called the Larmor frequency

$$f = \frac{\gamma}{2\pi} B_0 \quad (2.1)$$

where γ is the gyromagnetic ratio, a known constant for each type of atom.

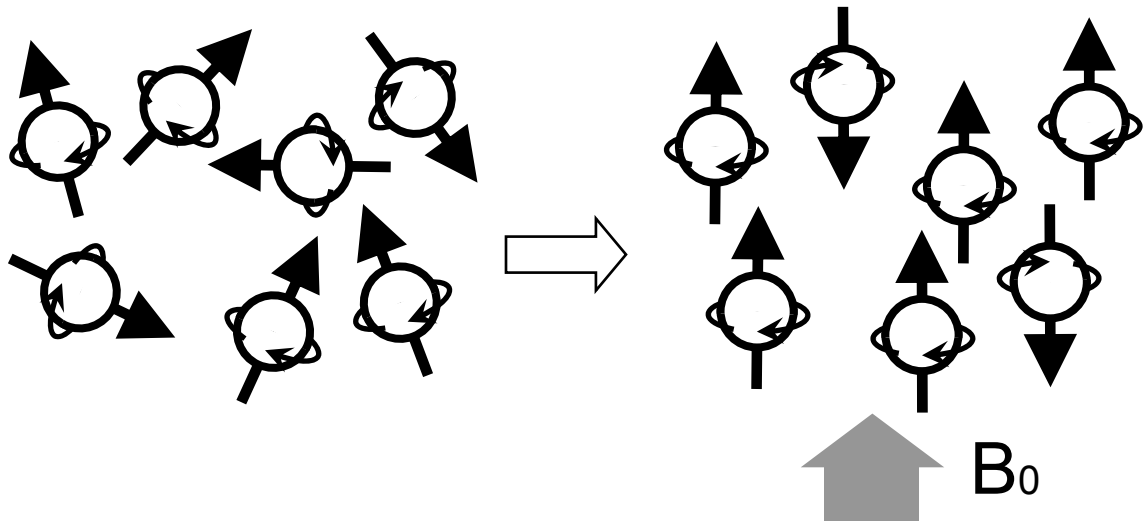


Figure 2.1. Polarization of magnetic spins. **Left:** Spins are randomly oriented under normal condition. **Right:** With the external magnetic field B_0 , two effects occur; (1) spins are aligned with the direction of B_0 , (2) spins exhibit resonance around B_0 at a known resonance frequency.

The net magnetic moment of the spin ensemble per unit volume is referred to as magnetization, denoted as \mathbf{M} . Macroscopically, the magnetization is also aligned with the direction of B_0 and rotates around B_0 at the Larmor frequency (see Figure 2.2). The direction of rotation can be found using left hand rule: when left hand's thumb points in the magnetic field direction, the fingers point in the precession direction.

In practice, resonance frequency is not spatially uniform. The sources of resonance offset include intrinsic inhomogeneity of the B_0 magnetic field, susceptibility difference between tissues, and chemical shift. The total off-resonance is determined by superposition of all these contributions, and plays important factor in MRI imaging.

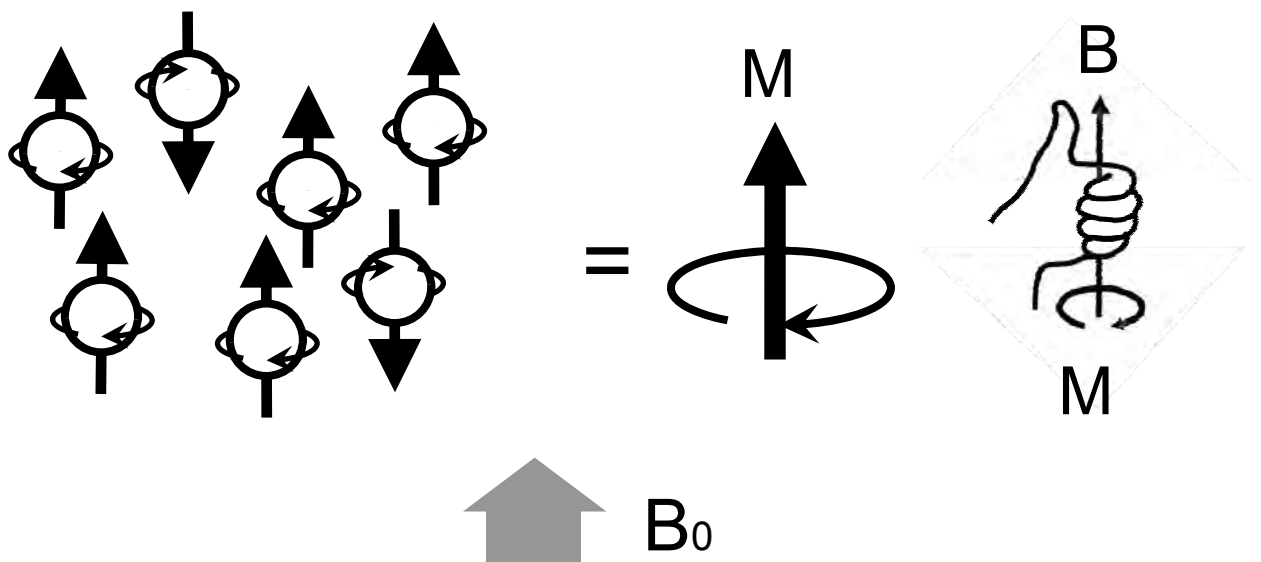


Figure 2.2. Illustration of magnetization. Magnetization is aligned with B_0 at equilibrium and rotates around B_0 based on left hand rule. When thumb points in the magnetic field direction, the fingers point in the precession direction.

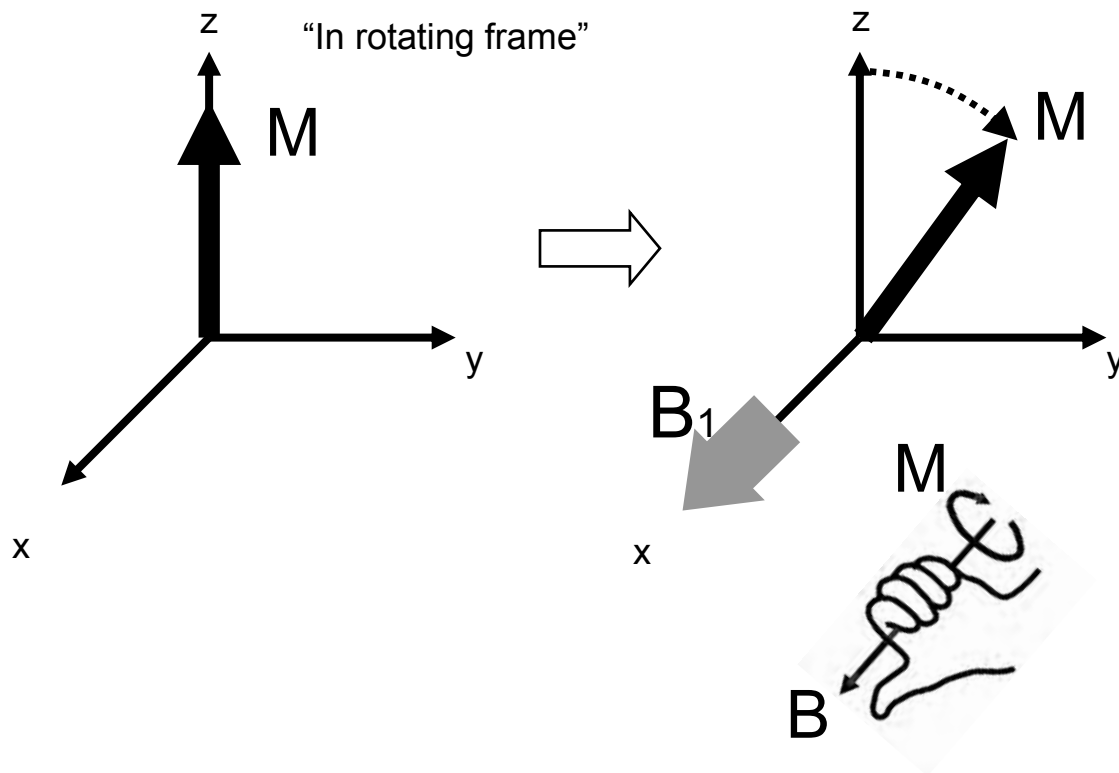


Figure 2.3. Magnetization excitation viewed in the rotating frame. The direction of rotation caused by B_1 can be found using the same left hand rule as used with B_0 .

2.1.2 Excitation

In the presence of a static magnetic field B_0 , the magnetization can be manipulated by an extra magnetic field B_1 . This magnetic field is applied using a radiofrequency (RF) pulse tuned to the resonance frequency in the plane perpendicular to B_0 . To simplify the further explanation, consider a frame that rotates at the same frequency of B_1 which is typically the same as Larmor

frequency [6]. All the notation will be based on rotating frame from here on. In this rotating frame, the magnetic field B_1 appears to have a constant vector direction, and B_0 does not exist. The magnetization is rotated around the direction of B_1 based on the same left hand rule and Eq. 2.1 (see Figure 2.3). This rotation of magnetization caused by B_1 is referred to as excitation. By manipulating $B_1(t)$, a particular angle of excitation can be achieved. Typically, a small tip ($\leq 50^\circ$) excitation is used in imaging acquisition, but flip-angle as large as 180° can be required in certain sequences. Figure 2.4 illustrates examples of 90° excitation and 180° excitation (or inversion).

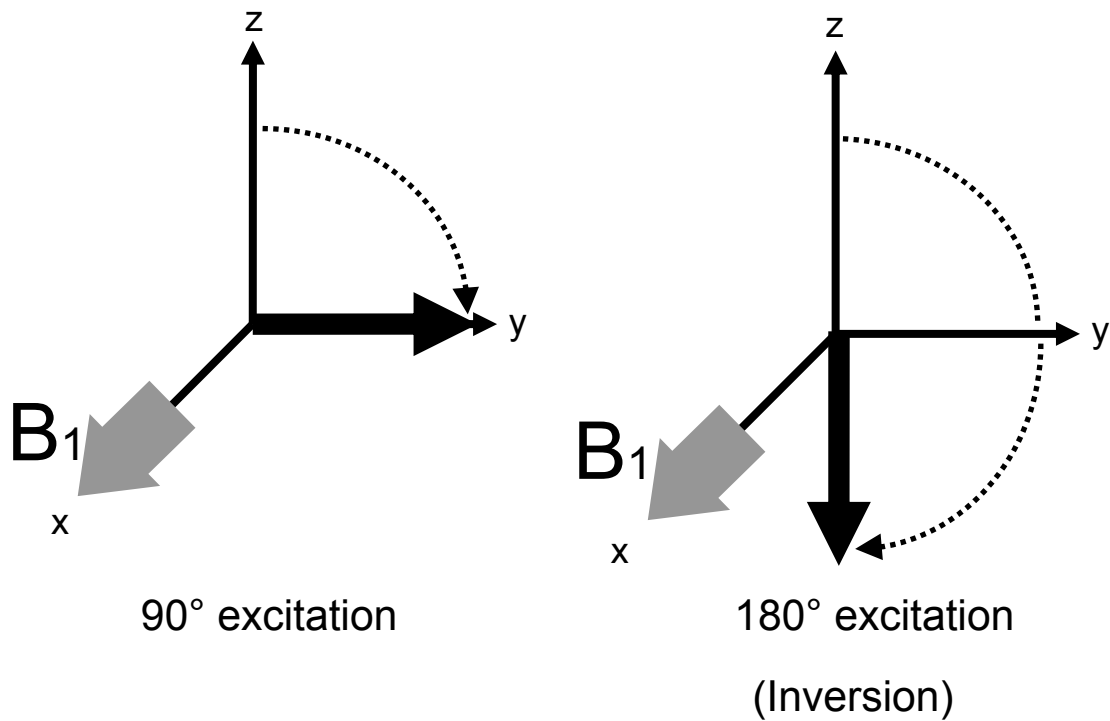


Figure 2.4. Illustration of 90° excitation and 180° excitation (or inversion). B_1 determines the flip-angle of excitation.

There exists imperfection in the applied B_1 magnetic field. This B_1 inhomogeneity is problematic in image acquisition because the offset changes excitation flip-angle, leading to spatial variation of signal intensity and contrast change in the images. In certain sequences, it is critical to achieve uniform excitation with exact flip-angle such as 90° or 180° regardless of B_1 variation. Adiabatic pulses are the class of RF pulses that were invented to meet this requirement [28, 34, 69, 79, 87]. In adiabatic excitation, B_1 field has a time-dependent amplitude $A(t)$ and a time-dependent carrier frequency $\omega_{rf}(t)$:

$$B_1(t) = A(t)e^{-i\omega_{rf}(t)t} \quad (2.2)$$

In a rotating frame whose angular frequency equals $\omega_{rf}(t)$, the effective magnetic field \mathbf{B}_{eff} can be decomposed into two orthogonal components. The transverse component of \mathbf{B}_{eff} is the envelope of the pulse,

$$B_y(t) = A(t) \quad (2.3)$$

where the B_1 field is initially applied along y-axis. The longitudinal component of \mathbf{B}_{eff} is

$$B_z(t) = \frac{\omega - \omega_{rf}(t)}{\gamma} \quad (2.4)$$

where ω is the resonance frequency ($\omega = \gamma B_0$). The effective magnetic field \mathbf{B}_{eff} is the vector sum of these two components. By applying sine waveform in $A(t)$ and cosine waveform in $\omega - \omega_{\text{rf}}(t)$, one can achieve \mathbf{B}_{eff} that sweeps from $+z$ axis to $-z$ -axis on yz -plane as shown in Figure 2.5. With this RF pulse, magnetization is effectively locked to \mathbf{B}_{eff} by rapid rotation around it and follows the passage of \mathbf{B}_{eff} , provided that the direction of \mathbf{B}_{eff} does not change fast compared to the angular frequency of magnetization rotation along \mathbf{B}_{eff} [74]. This condition known as the adiabatic condition is described by

$$\left| \frac{d\psi}{dt} \right| \ll \gamma |\mathbf{B}_{\text{eff}}| \quad (2.5)$$

where $\psi = \arctan(B_Y(t)/B_Z(t))$. Figure 2.5 illustrates 180° excitation using adiabatic pulse. Adiabatic excitation with 90° can be achieved by modifying and composing multiple of these segments [28, 89, 91].

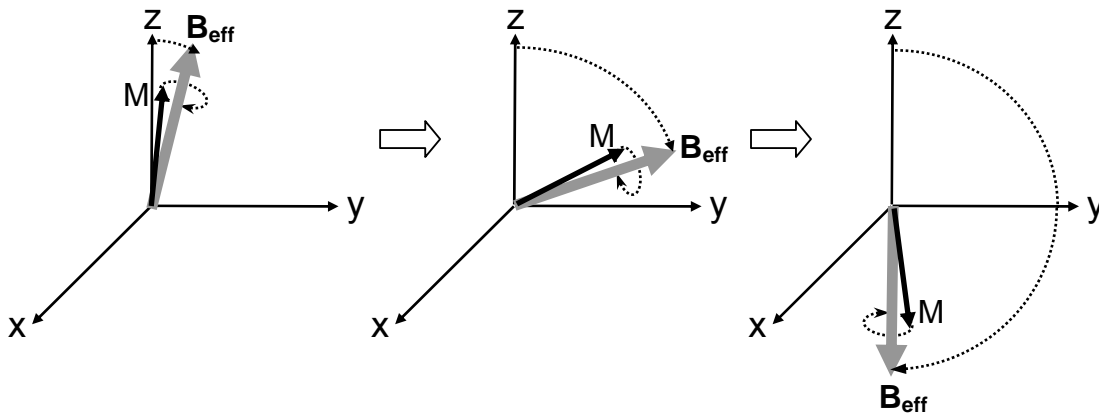


Figure 2.5. Illustration of adiabatic excitation for 180° flip-angle (inversion). Magnetization is effectively locked to \mathbf{B}_{eff} by rapid rotation around it, and follows the passage of \mathbf{B}_{eff} .

2.1.3 Relaxation

Following excitation, magnetization returns to its thermal equilibrium position. This mechanism is called relaxation and is characterized by two or more time constants for each tissue. Relaxation can be described in two components; longitudinal component that is parallel to B_0 field and transverse component that is perpendicular to B_0 field.

The longitudinal component of the magnetization M_Z and the transverse component of the magnetization M_{XY} behave according to Eq. 2.6 and Eq. 2.7, respectively.

$$M_Z(t) = M_0(1 - e^{-t/T_1}) + M_Z(0)e^{-t/T_1} \quad (2.6)$$

$$M_{XY}(t) = M_{XY}(0)e^{-t/T_2} \quad (2.7)$$

where M_0 is the magnitude of magnetization at its equilibrium state, and T_1 and T_2 are the time constants that specify the relaxation of longitudinal and transverse components of the magnetization, respectively. Figure 2.6 shows the example relaxation behavior of blood and myocardium at 3T ($T_1/T_2 = 1512$ ms/141 ms for blood and $T_1/T_2 = 1115$ ms/41 ms for myocardium [7]) after 90° excitation. The overall behavior of magnetization that is regulated by magnetic field and relaxation can be described by the following Bloch equation.

$$\frac{d\mathbf{M}}{dt} = \mathbf{M} \times \gamma \mathbf{B} - \frac{M_x \hat{i} + M_y \hat{j}}{T_2} - \frac{(M_z - M_0) \hat{k}}{T_1} \quad (2.8)$$

where \hat{i} , \hat{j} , and \hat{k} are the unit vectors in x, y, and z, respectively.

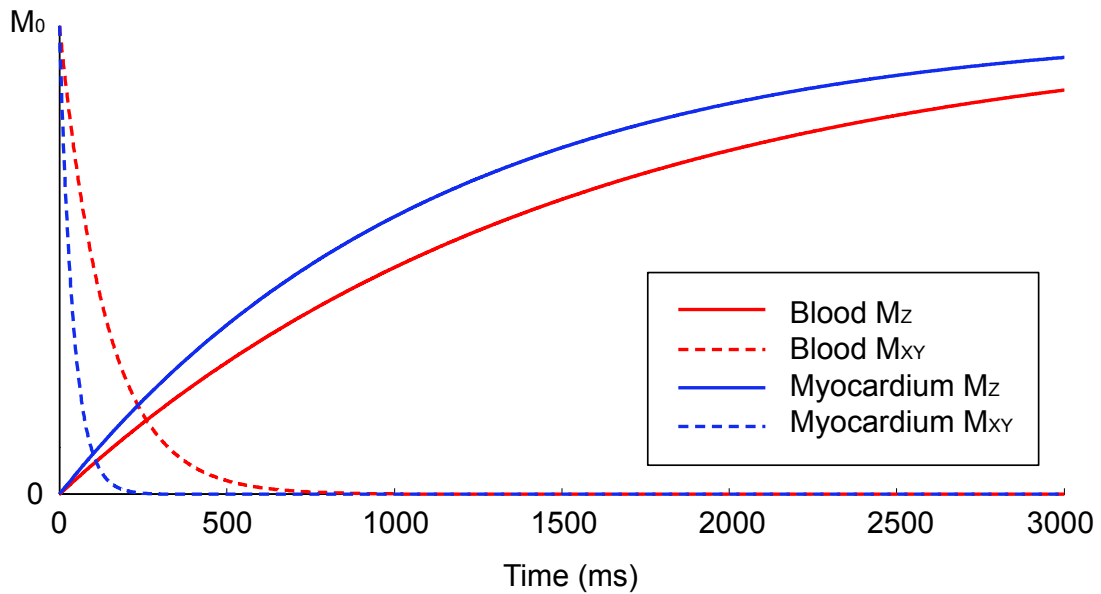


Figure 2.6. Relaxation behavior of longitudinal and transverse components of magnetization in blood and myocardium after 90° excitation. T_1/T_2 of the blood and myocardium are known to be 1512 ms/141 ms and 1115 ms/41 ms at 3T, respectively [7].

2.2 Myocardial Perfusion

2.2.1 Coronary Artery Disease

Coronary arteries are the small vessels that deliver oxygen-rich blood from the heart to its own muscle (myocardium). Coronary artery disease (CAD) is the end result of narrowing of the coronary arteries caused by accumulation of plaques within the vessel walls (see Figure 2.7). Narrowing or occlusion of the coronary arteries can reduce blood flow to the myocardium, possibly leading to chest pain, heart attack, arrhythmias, and heart failure. CAD is the single leading cause of death in the United States, accounting for approximately 500,000 deaths per year, and decreased quality of life for 13 million Americans [38]. Treatment is oriented towards the preservation of ventricular function and the prevention of progression. Three categories of diagnostic tests have been developed to assess the status of the heart: anatomical and functional tests that measure the efficiency of the pumping action of the myocardium; angiographic methods to evaluate the status of the coronary arteries; and approaches to assess myocardial perfusion and viability. These three types of data play important and complementary roles in the management of the cardiac patient.

- Assessment of ventricular function using measurements such as ejection fraction, ventricular volumes, regional wall motion, and valvular function provide a means to

determine the level of ventricular decompensation or failure, which guides the type and aggressiveness of treatment. Such measurements are provided most conveniently by echocardiography or more accurately by MRI.

- Imaging of the coronary arteries is a direct measure of the severity of CAD, for which the gold standard is X-ray angiography with cardiac catheterization, although less invasive methods are being developed.
- Imaging of myocardial perfusion indicates the presence and distribution of myocardial ischemia, and coupled with exercise, pharmacological stress, or vasodilation, can demonstrate regional perfusion reserve. Regional myocardial perfusion has long been evaluated using radionuclide imaging techniques such as SPECT and PET, and first-pass techniques based on MRI.

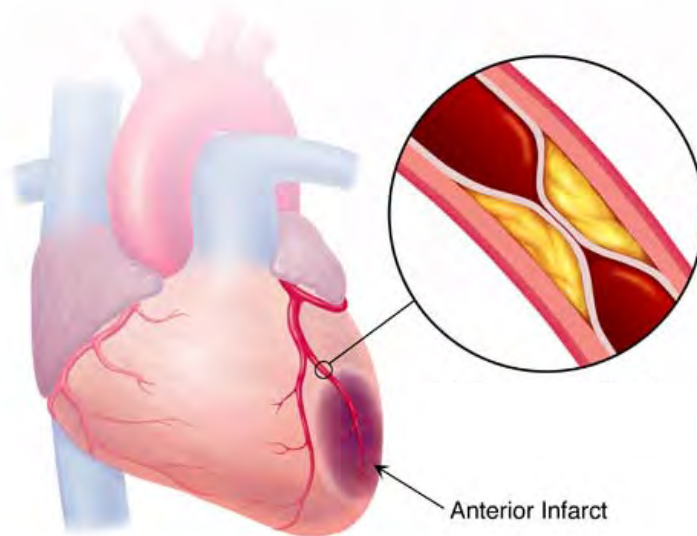


Figure 2.7. Illustration of narrowing of the coronary vessels due to accumulation of plaques within the vessel walls.

2.2.2 Myocardial Perfusion Imaging

Myocardial perfusion refers here to the general phenomenon of blood delivery to the myocardium. Myocardial blood flow (MBF) refers to the quantitative rate of delivery of blood to the myocardium (typically in ml-blood/g-tissue/min). MBF, along with exchange parameters, determine the rate of delivery of oxygen and nutrients to the myocardium, as well as the rate of clearance of waste products, and is thus a primary determinant of tissue viability.

Existing methods for myocardial perfusion imaging are useful but suboptimal. SPECT and PET scanning can provide measures of MBF but suffer from low spatial resolution (see Figure 2.8), and for this reason cannot reliably detect non-transmural perfusion deficits [71, 84]. The most widely used clinical SPECT protocols provide approximately 7-8 mm isotropic resolution. In addition, exposure to ionizing radiation poses a risk to the patient, and limits the use of these approaches for repeated or real-time scanning.

MRI-based first-pass methods are becoming widely used [46, 63, 84, 96] and provide a means to qualitatively assess myocardial perfusion with higher spatial resolution than SPECT. In these methods, a bolus of intravenous contrast agent is administered, and the first passage of the bolus through the heart is monitored by rapid dynamic imaging. From these dynamic data, MBF is calculated using the well-known deconvolution method [46]. First-pass methods, while promising, have key limitations that include unresolved artifacts (e.g. dark rim) [23], difficulties

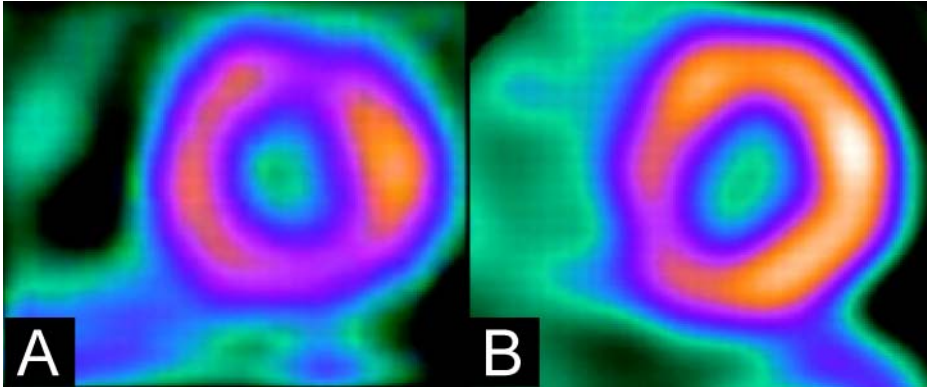


Figure 2.8. Examples of myocardial perfusion imaging with (A) SPECT and (B) PET [41].

with inter-observer variability [58] and absolute quantitation of MBF, and the toxic syndrome known as nephrogenic fibrosing dermopathy in patients with end-stage renal disease [86].

2.3 Arterial Spin Labeled MRI

2.3.1 Basic Concepts

Arterial spin labeling (ASL) is a powerful tool for the quantitative measurement of tissue blood flow using MRI, and has been primarily applied to the brain. The general idea of the technique is illustrated in Figure 2.9. In this technique, radiofrequency pulses are used to modify the longitudinal magnetization of arterial blood, generating an endogenous tag or tracer that decays

away with a time constant given by the T_1 relaxation rate (≈ 1.5 s for blood at 3 T [66]). After a delay to allow tagged blood to flow into the target tissue, an image (tagged) is acquired that reflects the inflow of tagged blood as well as static tissue in the slice. A second image (control) is then acquired in the absence of a preceding tag pulse. Figure 2.10 compares magnetizations in control and tagged images as a function of time. The inverted magnetization in tagged imaging returns toward the equilibrium state as explained in Section 2.1.3, and image acquisition is performed before the relaxation is completed. The magnetization difference between control and tagged images should appear in the difference image (control - tagged). This difference reflects the amount of tagged blood that has been delivered to the imaging region, and can be made directly proportional to local tissue blood flow.

ASL has several key advantages compared to other perfusion imaging techniques. First, the ASL signal is inherently and quantitatively related to tissue blood flow. Because the decay of the tag is rapid, images are acquired within a few seconds of the application of the tag. As a consequence, there is insufficient time for the tag to leave the target tissue by venous outflow. Exchange of tagged blood water with tissue water further decreases the likelihood of washout. This combination of factors results in a tracer technique in which the tag is effectively trapped in the target tissue, similar to the classic microsphere-based blood flow measurement. Secondly, ASL MRI is completely non-invasive, and does not require intravenous infusion of paramagnetic contrast agents or exposure to ionizing radiation. It therefore poses no risk to the patient (above that of a conventional MRI scan) and results in reduced cost and reduced side effects. For

example, ASL MRI could be safely applied in patients with end-stage renal disease who are not candidates for first-pass MPI.

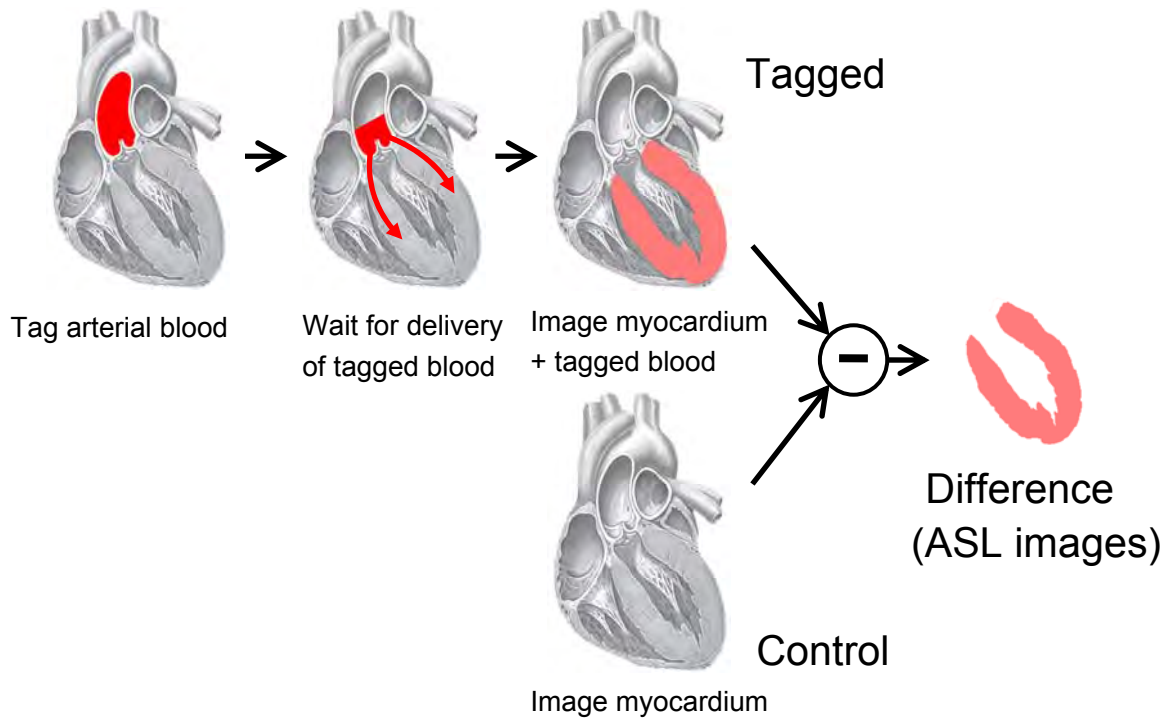


Figure 2.9. Generic diagram for ASL. ASL image is the difference of tagged (image with tagging) and control (image without tagging) images (figure courtesy of Eric Wong).

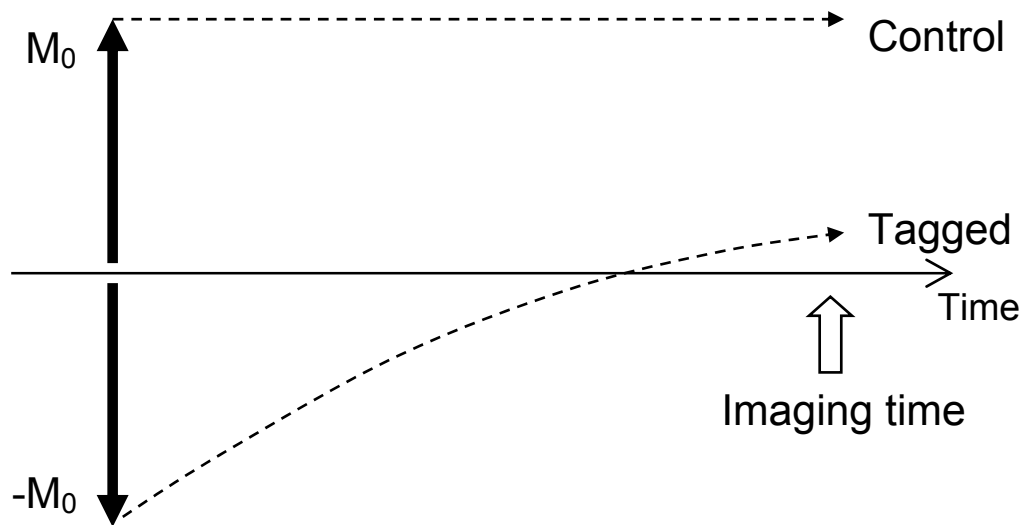


Figure 2.10. Illustration of arterial blood magnetization in control and tagged images as a function of time.

2.3.2 Pre-clinical Applications

ASL have been mostly used to measure regional cerebral blood flow [20] owing to less motion in brain. However, due to the recent discovery about nephrogenic systemic fibrosis (NSF) [86], the application of ASL in other body parts gained attention as an attractive alternative to perfusion imaging with contrast agent. A limited number of body ASL imaging have been successfully demonstrated in relatively static tissues such as skeletal muscle [102], lung [10, 75], and kidneys [25, 77]. Figure 2.11 shows example images of ASL from different body parts including brain.

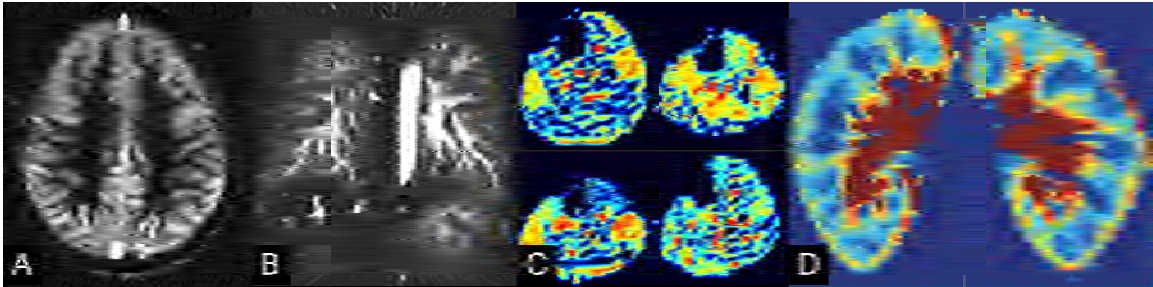


Figure 2.11. Example ASL images from brain (A), lung (B), lower legs (C) (courtesy of Eric Wong), and kidney (D) [25].

2.4 Myocardial ASL

2.4.1 Unique Challenges for ASL in the Heart

Compared to brain ASL, myocardial ASL faces several unique challenges. Cardiac motion requires the gating of tagging and imaging to appropriate portions of the cardiac cycle, and rapid imaging during the stable cardiac phases (mid-diastole or end-systole). It also limits the tag delay to an integer number of R-R intervals for most ASL tagging schemes. Respiratory motion requires the acquisition of tagged and control image pairs during the same breath-hold, during synchronized breathing, with navigator echo, and/or with careful image registration. The cardiac geometry complicates the location and timing of tagging, and leads to a high apparent ASL signal in the left ventricular (LV) blood pool with conventional tagging schemes. Finally, the intrinsic

myocardial signal-to-noise ratio (SNR) achieved with modern cardiac phased-array coils is roughly three times lower than the intrinsic gray matter SNR achieved with modern head coils, leading to a significant increase in the number of averages required for reliable tissue blood flow quantification.

2.4.2 Cardiac Physiology

For the purposes of the ASL measurement, the relevant features of the myocardial vascular physiology are 1) the transit delay to the microcirculation, 2) the exchange of water between blood and tissue water pools, and 3) the transit time through the capillary bed.

Transit delays, while they may be estimated from coronary angiography, will depend strongly on tagging geometry and timing, and can affect MBF quantitation [12]. In the brain, the transit delay allows for calculations and corrections for CBF. However, because the inflow of blood in the myocardium is pulsatile, the quantification of MBF, which is dependent upon the fraction of the tagged blood delivered in one cardiac cycle, is non-linearly related to the transit delay itself.

Water exchange affects the transition of the relaxation rate of the tag from the T_1 of blood to that of myocardium. Because the T_1 of myocardial tissue is shorter than that of blood, this is likely to have an effect on MBF quantitation. In most of ASL applications, it is assumed

that there is a complete water extraction from the vascular space to tissue immediately after arrival in the tissue, and the relaxation rate of tagged magnetization becomes that of tissue.

Capillary transit time influences the outflow of tagged blood into the venous circulation prior to image acquisition. The single pass extraction of water in the myocardial capillary bed is thought to be high ($\approx 95\%$) [5], and the capillary transit time is ≈ 0.9 sec [1]. This combination of parameters gives a mean transit time from arteriole to venule of tens of seconds (depending on the myocardial blood volume) and thus outflow of tagged blood is not likely to be an issue for myocardial ASL.

With these three considerations, the general kinetic model [12] that is widely used to describe cerebral blood flow in brain ASL studies, is entirely applicable to the description of MBF in myocardial ASL studies, and differs only in the values of the parameters.

2.4.3 Myocardial ASL in Animals

Previous attempts at myocardial ASL have been successful in small animals such as rats [52, 93, 97]. The advantages in small animals include: (1) SNR is high due to local radio frequency (RF) coils, (2) the intrinsic MBF values are at least 4 times higher than those of humans, leading to high SNR, and (3) heart rates are high, enabling apparent T_1 mapping [4] to be comfortably

performed (i.e., the T_1 recovery curve can be sampled at many time points, each during a stable cardiac phase).

2.4.4 Previous Studies on Myocardial ASL in Humans

Compared to myocardial ASL in small animals, the development of human myocardial ASL is still at an early stage [2, 9, 67, 73, 95, 98, 104, 108]. Preliminary studies have been mostly based on flow-sensitive alternating inversion recovery (FAIR) [49, 53], and differ in the models used for quantification and the methods used for breathing control and image acquisition. Wacker et al. [95] utilized apparent T_1 measurement after a saturation pulse (instead of an inversion pulse), which avoids the need for full relaxation between measurements, leading to reduced scan time and improved performance in the presence of irregular heart rates. Zhang and Northrup et al. acquired sets of images following a single inversion pulse for apparent T_1 measurement, accounting for magnetization saturation effects due to imaging excitation, and demonstrated this approach in dogs [104] and humans [67]. Poncelet et al. [73] utilized a quantification model derived from the Bloch equation, along with synchronized breathing, double-gating, and echo-planar imaging (EPI) image acquisition. A data fitting procedure was used to extrapolate the ASL signal from data acquired with different inversion times (caused by variations in heart rate). An et al. [2] employed a similar quantification model using FAIR tagging and balanced SSFP image

acquisition, and performed image acquisition in a pseudo-steady state, assuming constant heart rate. More recently, Blume et al. [9] used apparent T_1 mapping-based method with 4-fold acceleration technique. Despite these attempts, none have reported sufficient image quality and measurement consistency to provide useful diagnostic information in individual patients.

2.4.5 Myocardial ASL at 3 Tesla

Compared to 1.5 T, myocardial ASL performed at 3 T has several advantages. First, the equilibrium spin polarization is doubled, leading to direct two-fold increase in intrinsic SNR. Second, the T_1 relaxation time of blood is longer by roughly 30%. Longer T_1 delays the decay of the tag and preserves a larger ASL signal, for the same inversion time. Both of these effects dramatically increase the ASL signal, which is intrinsically quite low. Furthermore, 3 T is currently the highest field strength approved for clinical scanning by the FDA, making it easier to evaluate the methodology in patients.

In contrast, myocardial ASL at 3 T also has disadvantages such as RF heating, off-resonance, and B_1 inhomogeneity, all of which are general difficulties in cardiac imaging at 3 T. SAR (specific absorption rate) is the indicator of unwanted heating due to RF energy deposition, and is a constraint in most of imaging at 3 T. A careful selection of RF pulse is required to reduce RF power deposition. While SAR is the issue related to patient safety in MRI, off-resonance and

B_1 variations are imaging constraints that cause image artifacts or loss of SNR efficiency. Off-resonance is doubled at 3 T, and this limits many imaging sequences. For example, repetition time (TR) ≤ 3.8 ms is required to avoid banding artifacts in SSFP imaging sequence [80]. B_1 variation ranges up to 63% in the entire LV volume at 3 T [90]. In most of ASL experiments, tagging is realized by adiabatic inversion to achieve the maximum and uniform tagging efficiency regardless of B_1 variation. In-vivo optimization of parameters in adiabatic pulse is required in myocardial ASL.

Chapter 3

Graphical Analysis of Balanced Steady-state Free Precession

Balanced SSFP imaging (also known as True-FISP, FIESTA, or Balanced FFE) has emerged as a powerful and important imaging technique which provides exceptionally high signal-to-noise ratio (SNR) efficiency and useful T_2/T_1 -based contrast. This technique, originally proposed by Carr in 1958 [13] became practical only recently [19], due to the development of high-speed gradients that permit scanning with short repetition times. Balanced SSFP has found important applications in cardiovascular[64, 80], musculoskeletal [37], and neurologic imaging [62]. Furthermore, balanced-SSFP is a desirable imaging method in ASL techniques [2, 9, 48, 61, 108] because ASL-based perfusion imaging suffers from low intrinsic SNR. A matrix treatment of the balanced SSFP sequence can be used to find an exact solution for the steady-state signal [45], analyze transient response [36], and find the maximum signal amplitude on-resonance with its corresponding flip angle [82].

Compared to these matrix-based analyses, there has been little exploration into geometry-based analyses which often provide a more intuitive understanding. With similar

motivation, Dharmakumar et al. suggested a geometrical description of SSFP by identifying the steady-state locus of magnetization at the time immediately after each excitation pulse for a given set of imaging parameters [22]. In this chapter, we introduce a new graphical derivation of the steady-state signal in SSFP from a different perspective and provide a simple visualization of how the steady-state signal is affected by variation of the parameters, and matches known signal profiles (see Fig. 3.1). We introduce a new parameter “effective flip angle”, which is a unique determiner of signal strength in the steady state along with T_2/T_1 , and which effectively combines the effects of imaging flip angle and off-resonance precession. This offers a concise and intuitive picture of the balanced SSFP signal profile and how it can be manipulated. Unfortunately, we discovered later that this work overlapped in many parts with the paper from Schmitt [83] that was published a few months prior to us.

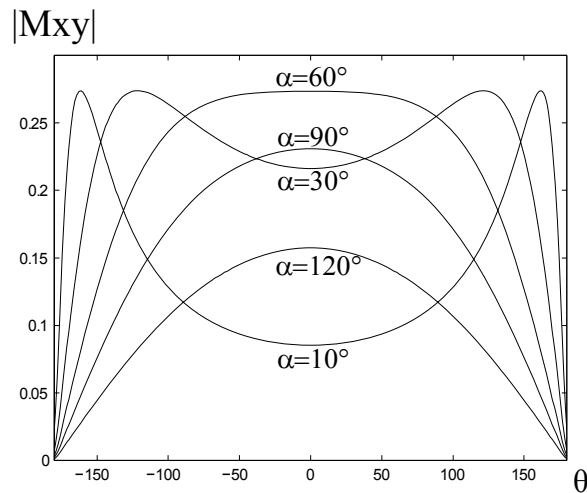


Figure 3.1. Alternating balanced SSFP profiles according to different flip angles for $T_1/T_2=1000\text{ms}/300\text{ms}$. θ denotes off-resonance precession within TR.

3.1 Matrix Analysis

SSFP imaging consists of a rapidly repeating sequence of excitations and acquisitions. Excitations have alternating sign, in order to ensure high signal on-resonance. In SSFP, all imaging gradients are rewound over the course of one repetition. The SSFP signal is highly sensitive to resonance frequency as shown in Figure 3.1, but provides superior SNR efficiency compared to gradient echo techniques.

There have been many works that derive the balanced SSFP signal using matrix analysis [11, 22, 26, 42, 115]. We will summarize this approach to find the solution that incorporates off-resonance. For the tip angle α and off-resonance precession angle θ within TR, let

$$\mathbf{A}_{\text{TR}} = \begin{bmatrix} E_2 & 0 & 0 \\ 0 & E_2 & 0 \\ 0 & 0 & E_1 \end{bmatrix} \quad (3.1)$$

$$\mathbf{b}_{\text{TR}} = \begin{bmatrix} 0 \\ 0 \\ M_0 \cdot (1 - E_1) \end{bmatrix} \quad (3.2)$$

$$\mathbf{R}_Y(\alpha) = \begin{bmatrix} \cos \alpha & 0 & -\sin \alpha \\ 0 & 1 & 0 \\ \sin \alpha & 0 & \cos \alpha \end{bmatrix} \quad (3.3)$$

$$\mathbf{R}_Z(\theta) = \begin{bmatrix} \cos \theta & \sin \theta & 0 \\ -\sin \theta & \cos \theta & 0 \\ 0 & 0 & 1 \end{bmatrix} \quad (3.4)$$

where $E_1=\exp(-TR/T_1)$, $E_2=\exp(-TR/T_2)$ and M_0 is the proton density. $\mathbf{A}_{TR}\cdot\mathbf{M}+\mathbf{b}_{TR}$ is a relaxed magnetization of \mathbf{M} after time TR, $\mathbf{R}_Y(\alpha)$ is a left-handed rotation matrix about y-axis by flip angle α , and $\mathbf{R}_Z(\theta)$ is a left-handed rotation matrix about z-axis by free precession angle θ . Then, the magnetizations at different timing in Figure 3.2 can be expressed as

$$\begin{aligned}
\mathbf{M}_2 &= \mathbf{A}_{TR} \cdot \mathbf{R}_Z(\theta) \cdot \mathbf{M}_1 + \mathbf{b}_{TR} \\
\mathbf{M}_3 &= \mathbf{R}_Y(-\alpha) \cdot \mathbf{M}_2 \\
\mathbf{M}_4 &= \mathbf{A}_{TR} \cdot \mathbf{R}_Z(\theta) \cdot \mathbf{M}_3 + \mathbf{b}_{TR} \\
\mathbf{M}_5 &= \mathbf{R}_Y(\alpha) \cdot \mathbf{M}_4
\end{aligned} \tag{3.5}$$

In the steady state, $\mathbf{M}_1=\mathbf{M}_5=\mathbf{M}_{SS}$ and Eq. 3.5 becomes $\mathbf{M}_{SS}=\mathbf{A}_{TR}\cdot\mathbf{M}_{SS}+\mathbf{b}_{TR}$. Therefore, $\mathbf{M}_{SS}=(\mathbf{I}-\mathbf{A}_{TR})^{-1}\cdot\mathbf{b}_{TR}$ where \mathbf{I} is a 3×3 identity matrix. The transverse component M_{XY} at echo time can be analytically expressed as

$$\begin{aligned}
M_{XY}(t=t_{TE}) &= M_{XY}(t=t_{SS}) \cdot \sqrt{E_2} \\
&= \frac{M_0 \cdot \sin\alpha(1-E_1)\sqrt{E_2(1+2E_2\cos\theta+E_2^2)}}{-E_1E_2\cos\alpha\cos\theta+E_2^2\cos\alpha-E_1\cos\alpha+E_2\cos\alpha\cos\theta-E_1E_2^2-E_1E_2\cos\theta+E_2\cos\theta+1}
\end{aligned} \tag{3.6}$$

Since $T_1, T_2 \gg TR$, the approximations $E_1 = \exp(-TR/T_1) \approx 1 - TR/T_1$ and $E_2 = \exp(-TR/T_2) \approx 1 - TR/T_2$ can be used to simplify Eq. 3.6 to

$$M_{XY}(t = t_{TE}) = \frac{M_0 \cdot \sin \alpha}{(1 - \cos \alpha) \cdot \frac{T_1}{T_2} \cdot \frac{1}{\cos \frac{\theta}{2}} + (1 + \cos \alpha) \cdot \cos \frac{\theta}{2}} \quad (3.7)$$

This is the signal strength solution from matrix derivation. M_{XY} is a function of α , θ , T_1 , T_2 , and M_0 . This will be compared with the result from our new derivation based on graphical analysis. A version of this equation for the on-resonance case ($\theta=0$) can be found in Ref. [22, 42, 82, 115].

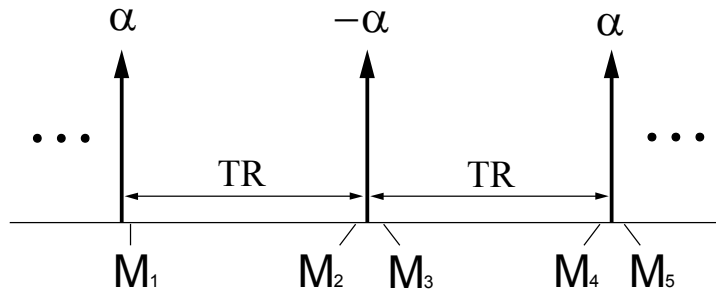


Figure 3.2. RF sequence of alternating balanced SSFP. M_X 's denote the vector magnetization right before or after the excitation. In the steady state, $M_5 = M_1$.

3.2 Graphical Analysis

3.2.1 On-resonance

In the case of alternating balanced SSFP exactly on-resonance ($\Delta f=0$), the magnetizations in the steady state are shown in Figure 3.3 (relaxation is exaggerated in this figure). The four magnetizations in Figure 3.3 all must have exactly the same magnitude; that is, $|\mathbf{M}(0)|=|\mathbf{M}(TR)|$. The variation of magnetization due to relaxation over one repetition can be expressed as

$$\Delta M_{XY} = M_{XY}(TR) - M_{XY}(0) = M_{XY}(0) \cdot (E_2 - 1) \quad (3.8)$$

$$\Delta M_Z = M_Z(TR) - M_Z(0) = (M_0 - M_Z(0)) \cdot (1 - E_1). \quad (3.9)$$

Let $M_{XY}(0) \approx M_{XY}(TR) \approx M_{XY}(TE) = M_{XY}$ and $M_Z(0) \approx M_Z(TR) \approx M_Z(TE) = M_Z$ since the disposition caused by relaxation is negligible. Again, if $T_1, T_2 \gg TR$, the approximations $E_1 = \exp(-TR/T_1) \approx 1 - TR/T_1$ and $E_2 = \exp(-TR/T_2) \approx 1 - TR/T_2$ can be used, and Eq. 3.8 and 3.9 become

$$\Delta M_{XY} = -M_{XY} \cdot (TR/T_2) \quad (3.10)$$

$$\Delta M_Z = (M_0 - M_Z) \cdot (TR/T_1) \quad (3.11)$$

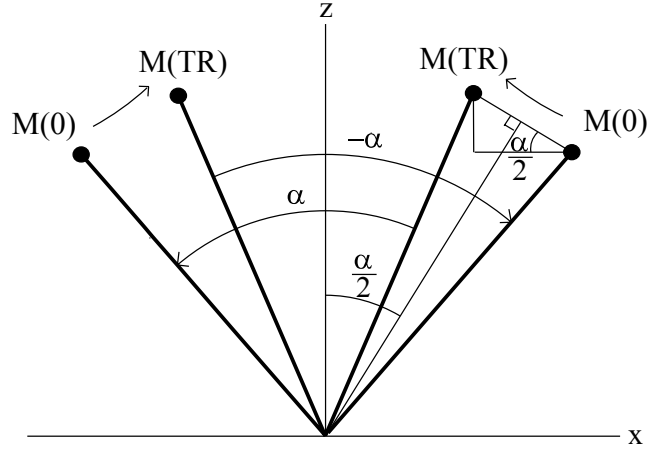


Figure 3.3. Steady-state magnetizations of alternating balanced SSFP on resonance with exaggerated relaxation. Symmetry about z-axis requires that the four magnetization vectors have the same magnitude, which means that $(\Delta M_{XY}, \Delta M_Z)$ from relaxation must be perpendicular to the magnetization position vector (M_{XY}, M_Z) .

The key observation is that the relaxation direction vector $(\Delta M_{XY}, \Delta M_Z)$ must be perpendicular to the magnetization position vector (M_{XY}, M_Z) in order to preserve magnitude. This would not necessarily be true if the four magnetizations have a different magnitude in the figure. The perpendicularity yields the following equation,

$$\begin{aligned}
 \frac{M_{XY}}{M_Z} &= \tan \frac{\alpha}{2} = \frac{\Delta M_Z}{-\Delta M_{XY}} \\
 &\approx \frac{M_0 - M_Z}{M_{XY}} \cdot \frac{T_2}{T_1} \\
 &= \frac{M_0 - \frac{M_{XY}}{\tan \alpha / 2}}{M_{XY}} \cdot \frac{T_2}{T_1}.
 \end{aligned} \tag{3.12}$$

Therefore,

$$M_{XY} = \frac{M_0 \cdot \sin \alpha}{(1 - \cos \alpha) \cdot \frac{T_1}{T_2} + (1 + \cos \alpha)}. \quad (3.13)$$

This matches Eq. 3.7 with $\theta=0$. M_{XY} is independent of TR but a function of (T_1/T_2) , α , and M_0 .

The relationship between M_{XY} and M_Z without α can also be derived from Eq. 3.12.

$$M_{XY}^2 \cdot \frac{T_1}{T_2} + \left(M_Z - \frac{M_0}{2} \right)^2 = \left(\frac{M_0}{2} \right)^2 \quad (3.14)$$

which is an elliptic equation. The trajectory of (M_{XY}, M_Z) in the steady state is shown as a function of α in Figure 3.4. This ellipse pattern was shown by Hennig et al. [40] in a description of the transition to steady state, and now has an intuitive explanation. The transition can be thought of as a process of moving along $\alpha/2$ line to find the equilibrium point where the relaxation vector and $\alpha/2$ line are perpendicular to each other. From Figure 3.4, one can see that the greatest possible transverse signal amplitude $M_0 / 2 \cdot \sqrt{T_2 / T_1}$ is achieved when (M_{XY}, M_Z) reaches the rightmost point, at which

$$\tan \frac{\alpha}{2} = \sqrt{\frac{T_2}{T_1}}$$

or

$$\cos \alpha = \frac{T_1 - T_2}{T_1 + T_2} \quad (3.15)$$

This explains that the alternating SSFP signal strength on resonance increases and then decreases after some point as the imaging flip angle is increased. Equation 3.15 is equal to Eq. 3.3 in Ref. [82]. The maximum transverse signal for balanced SSFP confirms T_2/T_1 contrast.

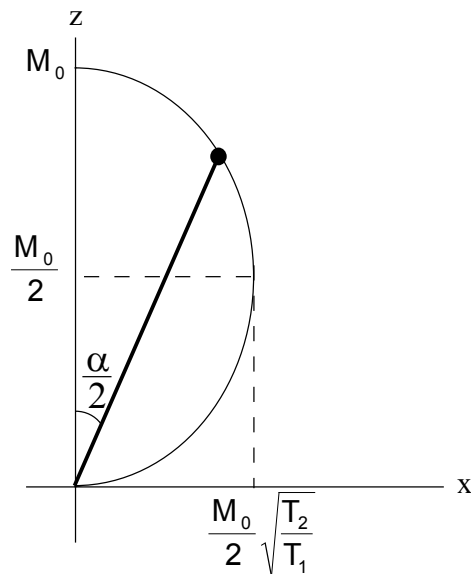


Figure 3.4. Magnetization (M_{xy} , M_z) in the steady state as a function of α . When magnetization reaches the rightmost point of the ellipse, the greatest transverse signal is produced.

3.2.2 Off-resonance

Now, we introduce off-resonance to the graphical analysis of alternating balanced SSFP, and let the dephasing angle within TR be θ . Figure 3.5a shows the path that SSFP magnetization follows in the steady state. All the magnetizations are refocused at $TE=TR/2$ regardless of off-resonance [81]. To consider the magnetization at the echo as shown in Figure 3.5, the two magnetizations are forming angle α' which is equivalent to the sum of two angles between the z-axis and each magnetization before and after the RF tip in Figure 3.5a under the assumption that the effect of relaxation is negligible during TE. The balanced SSFP with off-resonance can now be modeled as a balanced SSFP on-resonance but with effective flip angle α' . It can be geometrically shown that

$$\tan \frac{\alpha'}{2} = \frac{\tan \frac{\alpha}{2}}{\cos \frac{\theta}{2}}. \quad (3.16)$$

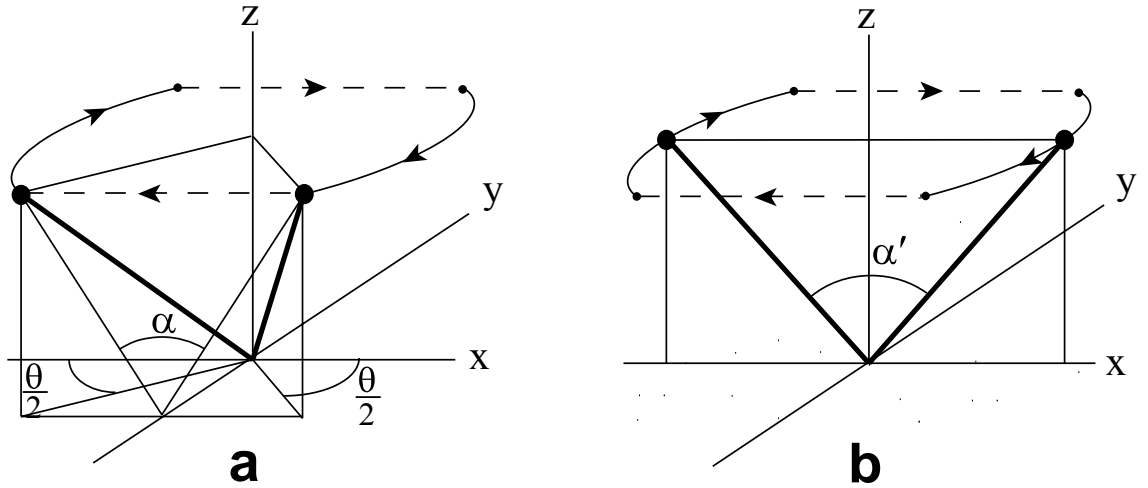


Figure 3.5. Balanced SSFP with off-resonance precession in the steady state. Solid and dotted arrows denote precession and instant excitation respectively. **a:** Magnetizations immediately before and after RF pulse. **b:** Magnetizations at $TE=TR/2$. The effective flip angle α' is equivalent to the sum of two angles that each magnetization in **a** forms with z-axis.

Therefore, the balanced SSFP magnetization at $TR/2$ with off-resonance will still lie along the same curve shown in Figure 3.3, but with effective flip angle α' as opposed to α . Substituting α' for α in Eq. 3.13 and plugging in Eq. 3.16, Eq. 3.13 becomes

$$M_{xy} = \frac{M_0 \cdot \sin \alpha}{(1 - \cos \alpha) \cdot \frac{T_1}{T_2} \cdot \frac{1}{\cos \frac{\theta}{2}} + (1 + \cos \alpha) \cdot \cos \frac{\theta}{2}} \quad (3.17)$$

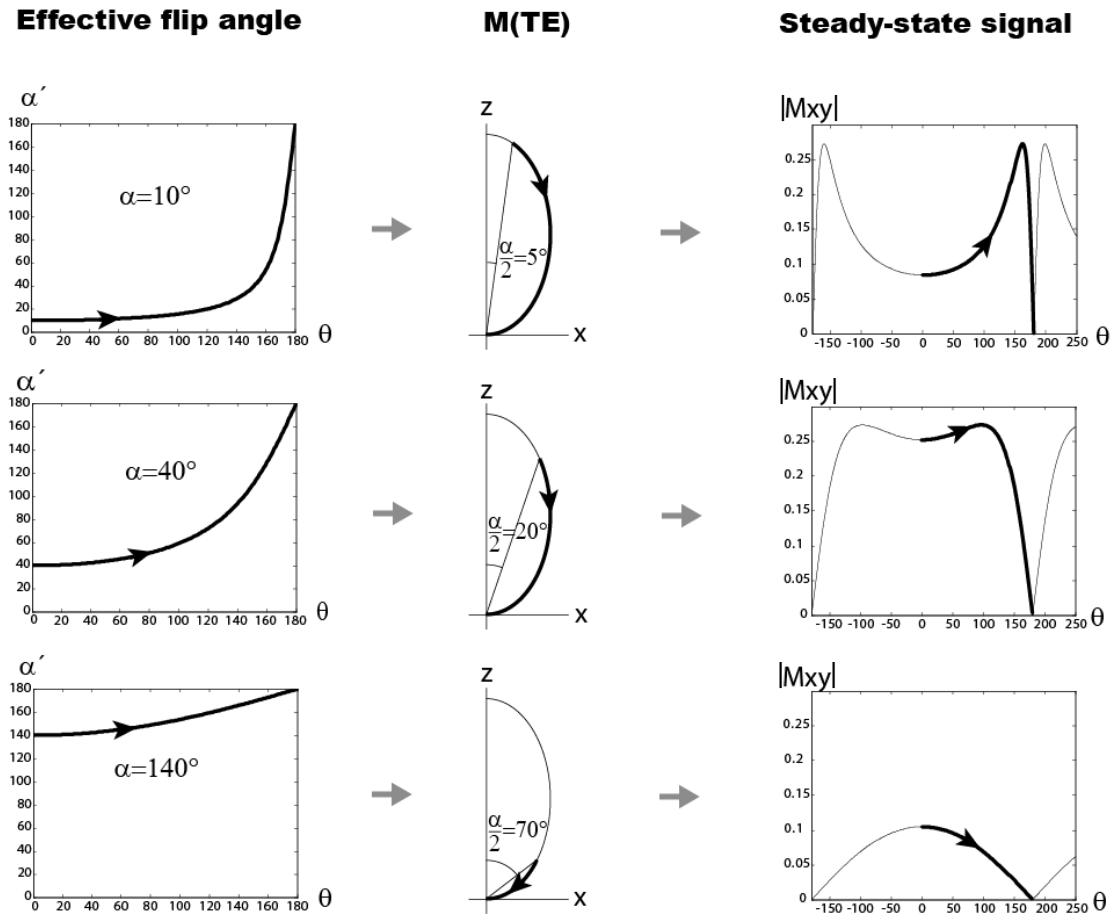


Figure 3.6. Effective flip angle, magnetization at echo time, and steady-state signal as a function of prescribed flip angle and off-resonance θ . For $\alpha=10^\circ$ (top row), $\alpha=40^\circ$ (middle row), and $\alpha=140^\circ$ (bottom row), the figures show how the effective flip angle, $M(TE)$, and transverse component profile are related as off-resonance changes. $T_1=1000\text{ms}$, $T_2=300\text{ms}$, and $TE=TR/2$.

which is identical to the matrix derivation of Eq. 3.7. This α' can also be substituted for α in Eq. 3.15 to find the flip angle α that produces the maximum signal for the corresponding off-resonance. Equation 3.16 shows that the effective flip angle α' is a function of α and off-

resonance angle θ . On resonance, α' is the same as α , and as θ increases from 0° to 180° , α' also increases and reaches 180° . Figure 3.6 illustrates how the magnetization has different frequency profiles according to flip angle α . Since α' remains around its initial value α on-resonance and then increases towards 180° as θ increases, the corresponding magnetization along the M_{XY} - M_Z trajectory moves down slowly in the upper portion of semi-ellipse, and gets faster when going through the lower portion.

3.3 Discussion

While gradient echo (GE) sequences have precession due to off-resonance and gradient pulses, balanced SSFP only retains precession due to off-resonance because the total gradient area amounts to zero over each repetition interval. Therefore, what is left in balanced SSFP is off-resonance precession, RF excitation, and relaxation. Since relaxation is often neglected in most of MR excitation analysis, it is very tempting to believe that the banding profile of balanced SSFP is the result of balancing precession and excitation. However, in the steady state, T_1 and T_2 relaxation plays the critical role in determining the signal profile, in which the relaxation direction vector should be perpendicular to the magnetization vector. This produces the phenomenon of magnetization in the steady state always falling on an ellipse.

One exceptional case where the presented analysis as well as matrix derivation with approximation does not apply is when α is extremely small (less than 1°). According to Eq. 3.17 or Eq. 3.7, signal amplitude should be a zero at $\theta=180^\circ$ regardless of flip angle α , and thus show two peaks just adjacent to $\theta=180^\circ$ for very small α (Figure 3.7a). But the exact simulation without approximation demonstrates that only one small peak is observed at $\theta =180^\circ$ instead of two peaks as shown in Figure 3.7b. This can be explained by the fact that relaxation has a more dominant impact on the magnetization in this case. Relaxation was ignored when off-resonance SSFP was modeled as on-resonance SSFP in Figure 3.5 since it typically has negligible effect on the angle between z-axis and magnetization during precession. This is not true for extremely small α . Angle variation due to relaxation becomes significant because the initial angle is small, and therefore the magnetization no longer follows the model described in Figure 3.4.

We considered alternating SSFP [42], however, an almost equivalent graphical analysis can be applied to non-alternating balanced SSFP. Off-resonance angle ϕ for non-alternating SSFP can be viewed as $180^\circ-\theta$, where θ is off-resonance angle for alternating SSFP. Therefore, the signal profile of non-alternating SSFP is simply a 180° shifted version of that derived for alternating SSFP.

In conclusion, the balanced SSFP signal profile has been derived in a novel graphical manner. Geometry-based derivation not only gives a fresh intuition of SSFP but further demonstrates the critical role of relaxation on the SSFP signal strength. This graphical analysis could be used to analyze more complex SSFP such as ones that create oscillating steady states [65,

70, 94], and may be used to develop catalyzation sequences or to develop tailored excitations to maximize uniformity of the SSFP signal. When using balanced SSFP in myocardial ASL, it is important to minimize the signal fluctuation due to off-resonance (see Figure 3.1) because subtle signal change can interfere with inherently low ASL signal.

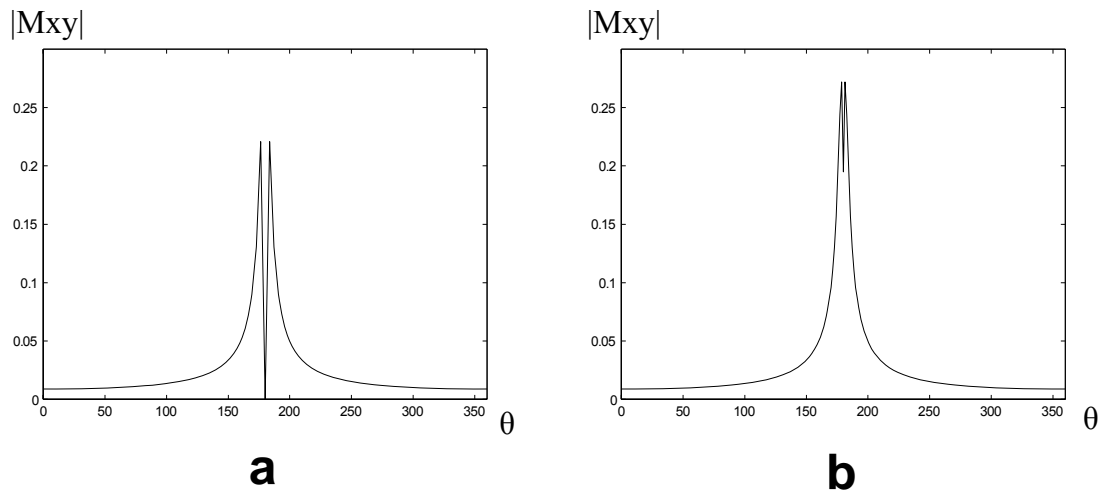


Figure 3.7. Signal profile based on graphical derivation or simulation with approximation (a) and the simulation without approximation (b) for extremely small flip angle. According to the exact simulation, one peak is observed at $\theta=180^\circ$ instead of two peaks.

Chapter 4

Feasibility of Myocardial Arterial Spin Labeling in Humans

In this chapter we demonstrate the feasibility of MBF measurement in humans, using breath-held cardiac-gated FAIR tagging and SSFP imaging at 3 Tesla, and present an analysis of thermal and physiological noise and their impact on MBF measurement error. Resting MBF measurements in ten healthy volunteers match ranges established using quantitative ^{13}N -Ammonia PET. The myocardial ASL signal was found to be inflow dependent, and was found to increase with passive leg elevation and isometric handgrip stress. We also determine that myocardial ASL is critically limited by physiological noise, which is an important challenge for further investigation.

4.1 Methods

4.1.1 Pulse sequence

Myocardial ASL was performed using a cardiac-gated FAIR-SSFP [2, 61] pulse sequence illustrated in Figure 4.1. FAIR tagging utilizes slab-selective and non-selective inversion pulses applied alternately to generate control images (without inversion of out-of-slice blood) and tagged images (with inversion of out-of-slice blood) respectively. Inversion and imaging are both centered at the same cardiac phase (mid-diastole, as determined by CINE scout scan) in successive R-R intervals such that the inversion slab contains the imaging slice, and the estimated MBF provides the average perfusion rate of pulsatile blood flow over one R-R interval. One pair of control and tagged images was acquired during a single breath-hold to minimize spatial mis-registration during subtraction. There was a 6-second time delay between the two image acquisitions, to allow for near-complete recovery of longitudinal magnetization. Six breath-holds (approx. 10-12 sec each) were performed to enable signal averaging of the tagged and control images. One short breath-hold (< 3 sec) was performed to acquire a baseline image (i.e. with no preparation) for quantification. The time delay between breath-holds was kept ≥ 15 seconds to ensure complete recovery of longitudinal magnetization. The subject's heart rate was monitored, and pulse timings were adjusted in real-time to follow the appropriate cardiac phase. To achieve complete cancellation of static tissue signal during subtraction, the inversion delay was kept

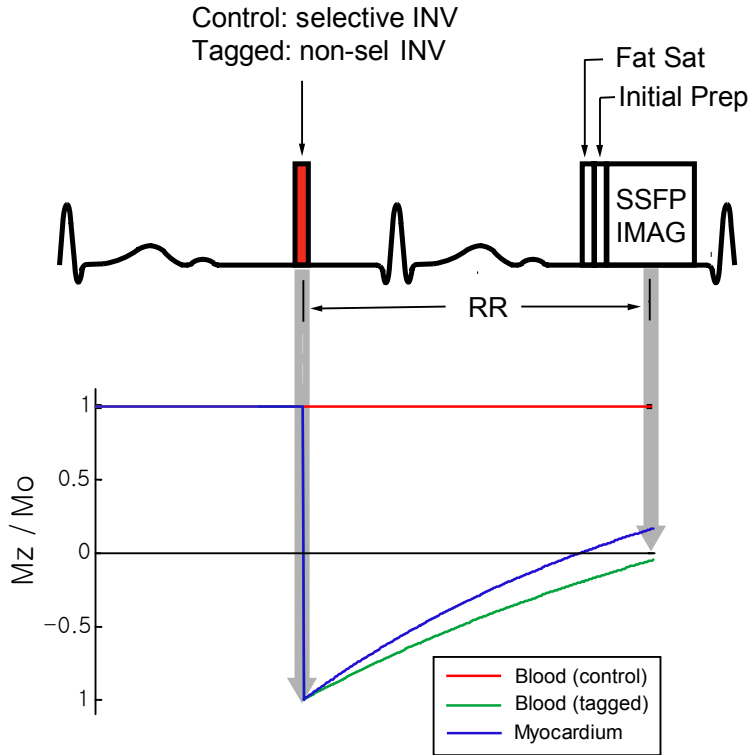


Figure 4.1. Myocardial ASL pulse sequence. Tagging and imaging are both centered at mid-diastole. Using Flow-induced Alternating Inversion Recovery (FAIR), preparatory inversion pulses are either slab-selective or non-selective to generate control or tagged images, respectively. Imaging is performed using a snapshot balanced steady-state free precession (SSFP) sequence that is preceded by fat saturation, to reduce signal from epicardial fat, and a 5-tip linear ramp preparation, to minimize transient signal oscillations. During each breath-hold, one control image and one tagged image are acquired with a 6-second pause in between.

identical for each image pair obtained in the same breath-hold. If there was a change in heart-rate during the breath-hold, the timing of the inversion pulse prior to the second image acquisition was shifted slightly, and for all practical purposes, still occurred during diastasis. The order of control and tagged image acquisition was alternated in each breath-hold and an even number of repetitions was used, in order to eliminate any bias due to incomplete recovery.

Image acquisition was performed using a snapshot 2DFT balanced SSFP sequence with 3.2 ms TR (total duration of 313 ms), 50° prescribed flip angle, and linear view ordering with full k-space acquisition. A 5-tip linear ramp was used to reduce signal oscillations during the transient SSFP acquisition [55]. In each study, a single mid-short axis slice was imaged using a 96×96 matrix over a 20-24cm isotropic FOV, with 10mm slice thickness. Acquisitions were prospectively gated using ECG or photo-plethysmograph signals. Inversions were achieved using adiabatic (hyperbolic secant) pulses because of their insensitivity to B_0 and B_1 variation (See Section 2.1.2). For slab-selective inversion, a thickness of 30 mm was used to trade off tolerance to slice profile imperfections and reduction of transit delay.

4.1.2 Reconstruction

Images were reconstructed using SENSE [76] with the reduction factor, $R = 1$, also known as Optimal B_1 Reconstruction (OBR) [32, 78]. Thus, SENSE reconstruction was used not for acceleration but to optimally combine signal from all coils and produce real-valued images that retain Gaussian image statistics even when the signal amplitude is close to zero. Note that in low SNR cases, sum-of-squares reconstruction results in image signal that follows a noncentral chi distribution. Coil sensitivity maps and the channel noise covariance matrix were obtained in a standard way [76] prior to ASL imaging.

4.1.3 Quantification

Regions of septal myocardium were manually segmented for each breath-hold, based on the difference signal (control – tagged). Regional MBF was estimated using following equation:

$$MBF = \frac{C - T}{2B \cdot RR \cdot e^{-RR/T_1} \cdot \rho} \quad (4.1)$$

derived from Buxton's general kinetic model [12], where C , T , and B refer to the mean myocardial signal on the region of interest in the control, tagged, and baseline images, RR represents the interval between two consecutive R waves, T_1 corresponds to T_1 of blood, and ρ is the normal myocardium density (1.053 g/ml). Signal averaging was performed over voxels within a region of interest as well as over multiple breath-holds to increase SNR.

4.1.4 Noise Analysis

Thermal Noise Analysis: Tagged and control images will each be corrupted by thermal noise, which will propagate to the MBF measurement. For Cartesian acquisitions, thermal noise is i.i.d. (independent and identically distributed) additive white Gaussian in the image domain. Consider σ_N , to be the noise standard deviation for each voxel in each source image (tagged and control). C

– T in Eq. (4.1) can be considered a random variable with a standard deviation $\sqrt{2} \cdot \sigma_N$ for each voxel. When signals are averaged over N_{avg} voxels (e.g. over a spatial region and/or multiple breath-holds), the standard deviation of $C - T$ becomes $\sqrt{2 / N_{avg}} \cdot \sigma_N$. Therefore, the measured MBF error (ΔMBF) is expected to follow a Gaussian distribution, with zero mean and standard deviation:

$$\sigma_{MBF,T} = \frac{\sqrt{2 / N_{avg}} \cdot \sigma_N}{2B \cdot RR \cdot e^{-RR/T_1}} \quad (4.2)$$

where variations in B can be neglected because of the high SNR of baseline images (> 40 in our studies). For given SNR, RR interval, and T_1 of blood, Eq. (4.2) relates the number of averages, N_{avg} to the distribution of measured MBF error. We calculated the minimum number of voxels to be averaged such that the measured MBF error is < 0.1 ml/g/min with $> 90\%$ confidence. With SNR = 70, heart rate = 60 bpm, and T_1 of blood = 1660 ms, this minimum number is about 300. In order to achieve close to this number of voxels over a septal ROI, we acquired six tagged and control image pairs during six breath-holds, with about 50 voxels in the prescribed ROI for each breath-hold for all scans. MBF measurement confidences were re-examined after the scan using the actual ROI sizes and the measured SNR for each subject.

Physiological Noise Analysis: One of the critical sources of errors in myocardial ASL is the physiological noise caused by metabolic fluctuation, respiratory and cardiac motion, and other

unknown variations over time. The variance of MBF measurements from each of the six breath-holds was calculated to estimate the temporal variation of the measurements. For the offset caused by alternating control/tagged imaging order to be excluded from the variance estimation, the variance of six measurements, σ_S^2 was calculated as follows.

$$\sigma_S^2 = \frac{\sigma_{odd}^2 + \sigma_{even}^2}{2} \quad (4.3)$$

where σ_{odd}^2 is a variance of average MBF from 1st, 3rd, and 5th breath-holds (tagged image acquired before control image), and σ_{even}^2 is a variance of average MBF from 2nd, 4th, and 6th breath-holds (control image acquired before tagged image). Based on the Gaussian model of physiological noise, the measured MBF error averaged from 6 breath-hold follows Gaussian distribution with zero mean and standard deviation:

$$\sigma_{MBF,P} = \frac{\sigma_S}{\sqrt{N_{BH}}} \quad (4.4)$$

where N_{BH} is the number of breath-holds, which was 6 for all scans. The probability of measured MBF error being < 0.1 ml/g/min was re-calculated using this distribution.

4.1.5 Experimental Methods

Experiments were performed on two 3 T whole-body short bore scanners (Signa Excite HD, GE Healthcare, Waukesha, WI) with gradients supporting 40 mT/m amplitude and 150 mT/m/ms slew rate. The body coil and an 8-channel cardiac array coil were used for RF transmission and signal reception, respectively. Each subject was screened and provided informed consent in accordance with institutional policy.

Resting MBF: Resting MBF measurements were performed in ten healthy volunteers (8 males/2 females, ages 28-35 years, heart rate 50-76 bpm). Five of the subjects were imaged twice on separate days, resulting in fifteen total scan sessions. No restriction was placed on exercise or caffeine/food intake prior to imaging.

Dependence on Inflow: In five healthy subjects, myocardial ASL scans were performed with three different tagging regions. In these three scans, the thickness of the selective inversion used for the control image was modified to include either: 1) only the imaging slice (3 cm thick), 2) the entire LV myocardium up to the aortic valve plane (12 cm thick), or 3) everything (nonselective). Increasing the thickness of the slab-selective inversion reduces the tagged blood volume, and is expected to reduce the measured MBF. Case 2 excludes blood already in the coronary vasculature. Case 3 excludes all blood, leading to an expected MBF measurement of zero.

Modulation with Mild Stress: In seven healthy subjects, myocardial ASL scans were performed at rest, and with two forms of mild stress: leg elevation and handgrip. For leg elevation, both the subjects' legs were passively elevated by 30-40 degrees to increase venous return. Leg elevation started 5 minutes before scanning and was maintained throughout the ASL scan. For handgrip stress, the subjects were asked to maintain isometric handgrip at 40% of maximum voluntary contraction (MVC) [39, 51]. Handgrip was initiated 1 - 2 minutes before each ASL scan, was maintained throughout the ASL scan, and was monitored by a handgrip dynamometer. MBF during handgrip is expected to be roughly 35% higher than at rest [56]. Aortic blood flow (ABF) during leg elevation is expected to be roughly 16% higher than at rest, which likely results in increased MBF as well [54]. For this study only, subjects were asked to refrain from caffeine or food intake for 4 hours prior to the scan, because these can increase resting MBF, and reduce the amount of MBF modulation caused by these stressors.

4.2 Results

4.2.1 Resting MBF

The measured resting MBF, standard deviation of MBF error, and confidences for MBF error < 0.1 ml/g/min based on thermal noise only and physiological noise, are summarized in Table 4.1.

The measured MBF range was 0.70 - 2.14 ml/g/min, which is consistent with the quantitative ^{13}N -Ammonia PET literature that has reported 0.73 - 2.43 ml/g/min as a range for asymptomatic human subjects [15]. The confidence based on thermal noise only was in a range of 70 - 99 %. This variation can be largely explained by the variation in intrinsic SNR and the variation in septal ROI size across subjects. The septal ROI size ranged from 1.35 to 6.53 cm³, where smaller septal ROIs were used in subjects with thinner myocardium. The confidence based on physiological noise was 18-94 % showing a substantially wider range compared to that of thermal noise. The standard deviation of MBF error due to thermal noise only and physiological noise were 0.065±0.018 ml/g/min and 0.218±0.115 ml/g/min respectively. The physiological noise is about 3.4 times higher than thermal noise although this value is affected by the size of ROI for each breath-hold. Note that the effect of thermal noise decreases systematically with larger ROI size, however this is not the case for physiological noise, as it is expected to have spatial correlation.

Figure 4.2 contains an illustration of the septal ROI, and a plot of resting MBF measurements from one volunteer (top row of Table 4.1) as a function of the number of voxels averaged. For this particular subject, the total number of voxels over six breath-holds was 483 and measured SNR was 74. With these parameters, the calculated probability of measured MBF error being < 0.1 ml/g/min was 96% based on thermal-noise only, but was 94% when accounting for physiologic noise.

Age, gender	MBF (ml/g/min)	SNR (B/ σ_N)	ROI size (cm ³)	Thermal noise only		Physiological noise	
				$\sigma_{MBF,T}$ (ml/g/min)	Confidence (%)	$\sigma_{MBF,P}$ (ml/g/min)	Confidence (%)
29 M	0.70	74	3.50	0.046	96	0.050	94
31 F	0.79	56	1.35	0.091	71	0.086	74
28 F	1.05	81	2.10	0.057	91	0.208	35
33 M	1.10	43	2.55	0.089	71	0.172	42
28 F	1.10	76	3.47	0.044	97	0.107	63
34 M	1.11	67	2.35	0.067	84	0.139	51
31 M	1.15	50	2.45	0.092	70	0.314	24
34 M	1.21	63	6.53	0.039	99	0.191	38
31 M	1.26	68	2.42	0.061	88	0.152	47
33 M	1.30	43	3.73	0.082	76	0.265	28
32 M	1.52	81	4.08	0.050	94	0.410	18
35 M	1.54	68	3.00	0.053	93	0.227	32
35 M	1.68	51	3.12	0.069	83	0.171	42
29 M	1.76	56	2.92	0.073	81	0.412	18
31 M	2.14	82	2.83	0.058	90	0.372	20
Avg.	1.29	64	3.09	0.065	86	0.218	42

Table 4.1. MBF measurements in healthy volunteers at rest. Columns contain the measured MBF, SNR, size of the septal ROI, standard deviation of measured MBF, and confidence (probability of measured MBF error being < 0.1 ml/g/min) from fifteen scans of healthy subjects. Data are sorted in ascending order according to measured MBF.

Figure 4.3 shows six MBF measurements averaged for each breath-hold in time order from the same subject. As specified earlier, the order of control and tagged image acquisitions alternated, with {tagged, control} in the odd breath-holds and {control, tagged} in the even breath-holds. Note that the MBF measurements from {tagged, control} pairs are always higher than those from {control, tagged} pairs. This error appears to stem from incomplete static tissue

cancellation due to time delay of 6 seconds, which is insufficient for the full relaxation of longitudinal magnetization. Based on Bloch simulation and Eq. (4.1), the MBF error caused by a 6 second time delay is ± 0.24 ml/g/min for the heart rate of this subject, which appears consistent with the pattern of oscillation seen in Figure 4.3. This effect is best seen in this particular dataset because it exhibited the lowest temporal noise of our 15 scans.

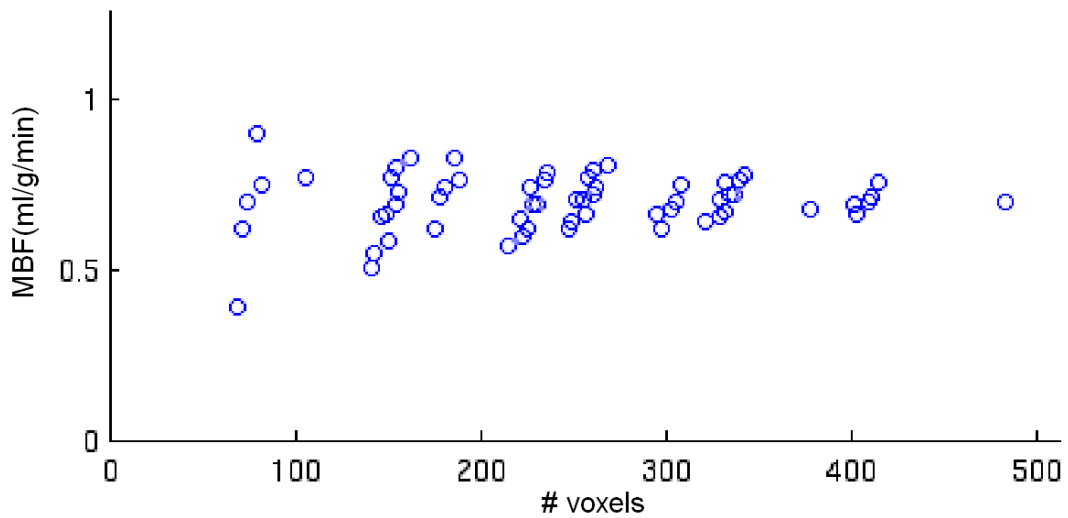


Figure 4.2. Measured resting MBF as a function of the number of voxels averaged. Roughly 80 voxels were segmented for each breath-hold, resulting in a measurement of 0.70 ml/g/min based on 6 breath-holds (right-most data point). All other data points were simulated by considering subsets of the 6 breath-holds.

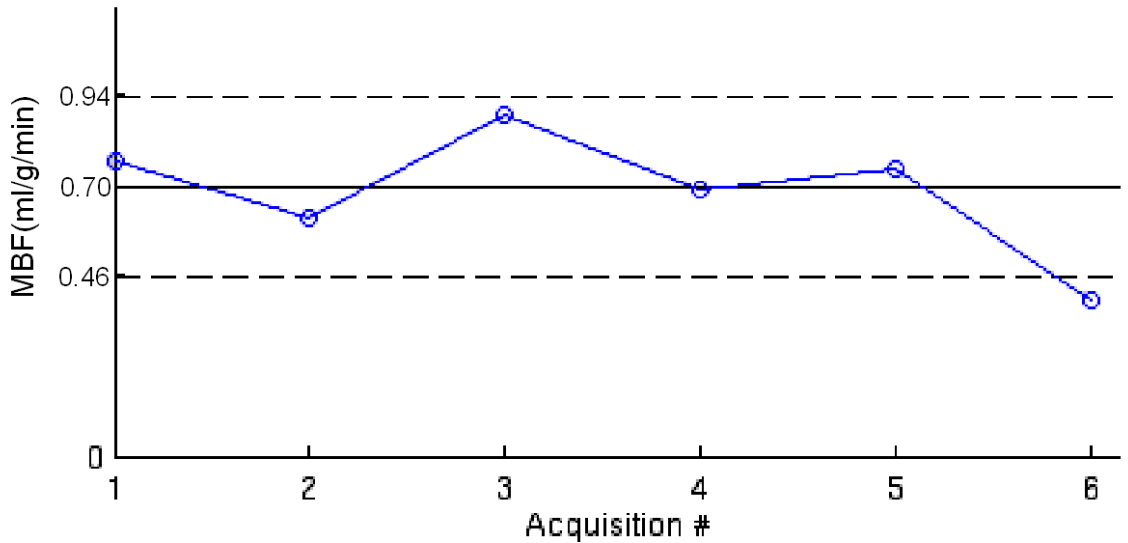


Figure 4.3. Six MBF measurements averaged for each breath-hold with alternating control/tagging image order. The solid line in the middle corresponds to the MBF value averaged over all voxels from six breath-holds (0.70 ml/g/min), and two dotted lines represent estimated upper (0.70+0.24 ml/g/min) and lower (0.70-0.24 ml/g/min) bounds of signal deviation due to incomplete static tissue relaxation.

4.2.2 Dependence on Inflow

Table 4.2 contains MBF measurements from five subjects where the thickness of the control image inversion slab was modified to include just the imaging slice, the entire left ventricle, and everything. In all subjects, thickening the inversion slab reduced measured MBF. The average change in MBF with inversion of LV and everything with respect to regular MBF were -68% and -92% respectively. This matched our expectation that excluding blood in the coronaries from tagging would result in lower estimated MBF than that from including all out-of-slice blood, and supports the notion that the ASL signal measured by this approach is dominated by inflow.

Age, gender	FAIR	Tag excludes LV		Null tag	
		MBF	Change	MBF	Change
31 M	1.15	0.34	-70%	0.16	-86%
28 F	1.10	0.61	-45%	0.10	-91%
29 M	1.76	0.79	-55%	-0.34	-119%
32 M	1.52	0.12	-92%	0.66	-57%
34 M	1.11	0.24	-79%	-0.07	-106%
Avg.	1.33	0.42	-68%	0.10	-92%

Table 4.2. MBF measurements (in ml/g/min) with different slab-selective inversion thicknesses (3 cm for slice, 12 cm for LV, and nonselective for everything).

4.2.3 Modulation with Mild Stress

Table 4.3 contains MBF measurements from seven subjects at rest and with two forms of mild stress, passive leg elevation and handgrip at 40% of MVC. The average heart rate change from rest was -1% with leg elevation and 0.3% with handgrip. MBF measurements during leg elevation and handgrip were higher than MBF measurement at rest in five subjects, comparable in one subject, and lower in one subject. The average increases in MBF were 30% and 29% with leg elevation and handgrip respectively. These results are comparable to those in Refs. [12] and [51] where ABF during passive leg elevation increased by roughly 16%, and MBF during handgrip increased by roughly 35%. The 29% increase of MBF with handgrip is statistically significant ($p=0.045$) while the 30% increase of MBF with leg elevation is not statistically significant ($p=0.157$), largely due to the outlier result from the fourth volunteer.

Age, gender	Resting MBF (HR)	Leg elevation		Handgrip	
		MBF (HR)	MBF Change	MBF (HR)	MBF Change
29 M	0.70 (62)	0.94 (60)	34%	0.93 (62)	32%
31 F	0.79 (50)	1.24 (52)	58%	1.19 (52)	51%
28 F	1.05 (68)	1.74 (71)	65%	1.49 (75)	41%
31 M	1.26 (64)	0.91 (68)	-28%	1.11 (64)	-12%
32 M	0.98 (68)	1.01 (64)	3%	1.24 (67)	27%
29 M	0.99 (66)	1.03 (56)	4%	0.96 (60)	-3%
32 M	0.47 (69)	0.83 (71)	74%	0.80 (68)	68%
Avg.	0.89 (64)	1.10 (63)	30%	1.10 (64)	29%

Table 4.3. MBF measurements (in ml/g/min) at rest, with passive leg elevation, and with isometric handgrip exercise, and heart rates (HR, in bpm) for each study. The average heart rate change from rest was -1% with leg elevation and 0.3% with handgrip.

4.3 Discussion

This study demonstrates that subtractive myocardial ASL at 3 Tesla with pulsed tagging and SSFP imaging yields a distinct and measurable signal in human myocardium. In healthy volunteers, this signal is consistent with MBF ranges established using ^{13}N -ammonia PET, and shows a tendency to be inflow-dependent and modulate as expected with mild forms of stress. This study supports the feasibility of quantifying MBF in humans non-invasively using arterial spin labeling.

This study has also determined that myocardial ASL MRI is limited by SNR. Although normal MBF is roughly twice as high as normal cerebral blood flow (CBF) [15, 44], the intrinsic myocardial SNR when using modern 8-channel cardiac coils is roughly 3 times lower than gray matter SNR when using modern 8-channel head coils (measured on our 3 T scanner in 3 healthy volunteers), primarily due to the larger noise-producing volume. This results in the need for a higher number of signal averages in myocardial ASL, compared to brain ASL, in order to achieve diagnostically useful confidence. Furthermore, because it is not practical to use 50+ repetitions in myocardial ASL (equal to the number of breath-holds), spatial signal averaging is also required. The current spatial resolution of our MBF measurements is roughly 3 cm^3 (much larger than the resolution of the base images, $2.5 \times 2.5 \times 10 \text{ mm}^3$) due to this need for spatial signal averaging.

As an alternative to voxelwise myocardial perfusion mapping, ROI-based analysis appears to be feasible, with segmental resolution similar to the standard 17-segment model [14]. Figure 4.4 contains a voxelwise perfusion map from one breath-hold, and a ROI-based perfusion map from 20 breath-holds for comparison, both from the same healthy volunteer that exhibited moderate physiologic noise ($\sigma_{MBF,P} = 0.066 \text{ ml/g/min}$ for the entire myocardium). For the ROI-based perfusion map, only endocardial and epicardial borders from each breath-hold were delineated manually based on the difference image, and the circumference of the LV was automatically divided into eight segments. Signal averaging was performed within each segment over multiple breath-holds, yielding one MBF estimate that represents each segment. This way,

even with the rather low SNR of myocardial ASL, the current approach may provide a perfusion map that is of diagnostic value, without requiring image registration for signal averaging.

Improvements in SNR efficiency will of course benefit ROI-based perfusion mapping, and will enable shorter scans, smaller ROIs, and tighter confidence intervals. Myocardial SNR is expected to be increased 50-75% with emerging 16 and 32 channel cardiac coils [35]. Furthermore the SNR of myocardial ASL can be expected to improve with the development of more efficient tagging schemes (specific to the heart) and with the development of image acquisition methods optimized for detecting the ASL signal, which both remain as future work.

Physiological noise (sometimes called temporal noise) is a crucial factor in myocardial ASL mostly due to breathing motion. Our preliminary estimates suggest that physiological noise in these studies was approximately 3.4 times higher than the level of thermal noise, which would suggest the use of far more than 6 breath-holds. However, the standard deviation of the physiological noise distribution over different subjects was also 6.5 times higher than that of thermal noise only. This indicates that the number of breath-holds needed for confidence in the derived MBF measurement will vary significantly across subject, while thermal noise is relatively consistent over different subjects and can yield < 0.1 ml/g/min error with 86% confidence with 6 breath-holds. This provides strong motivation for future investigation of background suppression (BGS) schemes and novel tagging schemes that have the potential to reduce physiological noise.

One important drawback of FAIR tagging (or any slab selective tag of the proximal aorta in the short axis plane) is that the tagged region includes blood in the left atrium and

possibly a portion of the left ventricle. This results in spurious ASL signal in the LV blood pool that may interfere with measurement of the myocardial ASL signal. The effect is most readily apparent in difference images, where the LV blood pool is typically 30-40 times brighter than adjacent myocardium. One possible solution is to apply diffusion sensitizing gradients (DSG) with low diffusion weighting to dephase blood flow [68] immediately prior to imaging acquisition in both control and tagged images. While this is a simple solution to suppress signal from the LV blood pool, it has a disadvantage that the tagged blood in myocardium experiences signal attenuation due to T_2 relaxation and motion related dephasing, leading to SNR loss. LV blood in the ASL difference image can also be suppressed by more sophisticated tagging scheme such as one that selectively excludes the left atrium and left ventricle while tagging the proximal aorta. Suppression of the LV blood signal is likely to reduce physiological noise and allow the use of larger myocardial ROIs while avoiding partial volume effects in voxels along the endocardial border.

Unlike brain ASL, image acquisition in the steady state is difficult for myocardial ASL because the duration of breath-holds is limited and the heart rate can vary during a scan session. We chose a multiple breath-hold strategy, where each breath-hold contained a pair of control and tagged images with time delay of 6 seconds between them. In order to compensate for MBF measurement error caused by incomplete relaxation, we alternated the order of control and tagged images, and used an even number of breath-holds. It is possible to use longer time delays between tagged and control images (e.g. 10 sec) to provide more complete relaxation, however this

increases the duration of each breath-hold, which increases the possibility of mis-registration and changes in the T_1 of blood due to deoxygenation. In our experience, alternating the order of the tagged and control images proved to be a simple and effective way to mitigate error caused by incomplete relaxation. Ultimately, free breathing methods employing advanced prospective gating and tracking may be necessary for routine application of myocardial ASL in patients.

Brain ASL has evolved over the past 15-20 years, and many important innovations can be applied to myocardial ASL. For instance, BGS has proved useful for the reduction of physiological noise in brain ASL [24, 27, 100, 103], and may also be beneficial in myocardial ASL where breathing motion is significant. Also, pseudocontinuous tagging [18, 101], which provides the highest tagging efficiency among existing brain ASL methods, may be applied to myocardial ASL, as a means to improve SNR. In this case, the spatial placement and the timing of flow-driven tagging pulses should be optimized to the coronary artery geometry and pulsatile flow pattern, in order to produce the highest tagging efficiency.

The validation of myocardial ASL in humans is complicated by cardiac and respiratory motions, and the lack of an established ground truth with which to compare the results from proposed method. This is quite different from animal studies, where sedation is possible and results can be compared with invasive microsphere-based blood flow measurement. A definitive validation of proposed methods against a gold standard such as ^{13}N -ammonia PET would be a natural follow up to this study.

In summary, we have demonstrated the feasibility of myocardial blood flow assessment in humans, using arterial spin labeling at 3 Tesla. MBF measurements in healthy volunteers at rest were consistent with MBF ranges established by the quantitative PET literature. These MBF measurements were inflow-dependent, and increased by 30% and 29% with passive leg elevation and handgrip stress respectively, as expected. This study also demonstrates that myocardial ASL is limited by SNR, and that accurate perfusion assessment with the technique is currently limited to region-of-interest analysis. Sources of physiological (non-thermal) noise and suppression techniques remain to be explored. There is substantial opportunity for improved tagging and imaging methods that may strengthen the myocardial ASL signal while reducing temporal noise.

Chapter 5

Measurement of Changes in Myocardial Perfusion with Vasodilatation

During stress induced by exercise, pharmacological stress, or vasodilatation, the MBF measurements are multiple times higher than those at rest. While resting MBF does not decrease until diameter of coronary arteries is reduced by 85%, perfusion reserve begins to decrease with stenosis of 30-45% where perfusion reserve is calculated as the ratio of MBF during stress to MBF at rest. Perfusion reserve has been proposed as an index of severity of a coronary lesion because it is impaired by CAD before the changes in resting MBF become manifest [30, 31]. In this chapter we applied myocardial ASL to the measurement of perfusion reserve in nineteen patients scheduled for cardiac magnetic resonance (CMR). Data was collected at rest and during intravenous infusion of adenosine [3, 95, 97]. We report the first perfusion reserve measurements with myocardial ASL that indicate that myocardial ASL is capable of detecting clinically relevant increases in MBF with vasodilatation [114].

5.1 Methods

5.1.1 Study Design

Nineteen patients (aged 65 ± 11 years, 14 women / 5 men) were recruited, among those who were suspected of having CAD and scheduled for stress CMR exams at the Loma Linda University Heart and Imaging Center. This study was approved by our Institutional Review Board, and each patient provided written informed consent. Rest and stress myocardial ASL scans were incorporated into the routine CMR protocol as showed in Figure 5.1. All ASL scans were performed before first-pass perfusion imaging to prevent residual gadolinium from reducing the T_1 of blood and confounding the computation of MBF from ASL images. Each ASL scan required six breath-holds and could be comfortably performed in 3 minutes. In most patients, two rest ASL scans were performed and averaged because the scan time was not limited at rest. Then the adenosine infusion was started using standard dosage (0.14 mg/kg/min). After 2 minutes, the stress ASL scan was performed. The average heart rates during rest and stress ASL scans were recorded independently. Immediately after the stress ASL scan, CMR first-pass perfusion was performed between minutes 5 and 6 of the adenosine infusion (total infusion duration = 6 minutes). During the infusion, the medical status of the patient was monitored by a nurse, and the patient was asked frequently if he/she felt any adverse symptoms of adenosine. The rest of the

CMR imaging protocol remained unchanged, and included late gadolinium enhancement and cardiac function CINE imaging. Based on the CMR results, patients who were suspected to have severe ischemic heart disease also underwent X-ray coronary angiography within one month.

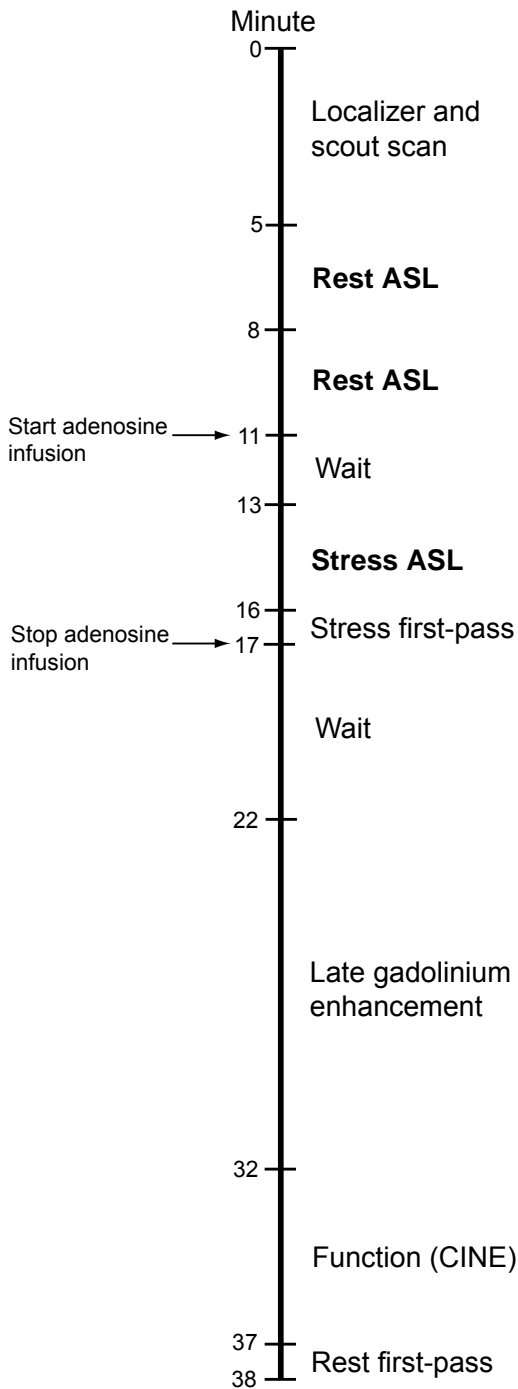


Figure 5.1. Modified stress CMR protocol. Myocardial ASL scans are performed at rest and during adenosine infusion, both prior to first-pass imaging to avoid confounding effects of the contrast agent (lowering the blood T_1). The CMR protocol after completion of adenosine infusion is unchanged and includes viability and function imaging.

5.1.2 Imaging Methods

Imaging method of myocardial ASL was the same as described in Chapter 4. A single mid short-axis slice was scanned using FAIR tagging and balanced SSFP imaging [108]. Tagging was achieved by applying nonselective and selective adiabatic inversions. Imaging was performed with snap-shot two-dimensional Fourier transform (2DFT) SSFP acquisition with TR = 3.2 ms (total duration = 313 ms), flip-angle = 50°, matrix size = 96 x 96 over 24-32 cm isotropic field of view (FOV), full k-space acquisition, and slice thickness = 1 cm. Parallel imaging was not used. Both tagging and imaging were performed at mid-diastole using ECG gating. The trigger delay was determined from a CINE scout scan. Each ASL scan required six breath-holds, with one pair of tagged and control images acquired in each breath-hold. Each breath-hold lasted 10 seconds, and the total scan time was 3 minutes including breaks.

The routine CMR first-pass perfusion sequence covered four short-axis slices using a saturation recovery fast gradient echo (FGRE) pulse sequence. The imaging parameters were: TR = 6.5 ms, flip-angle = 10°, matrix size = 128 X 128, and slice thickness = 1 cm. The intravascular contrast-agent (Gd-BOPTA, MultiHance, dosage: 0.05 mmol/kg) and saline flush (20 ml) was injected at a rate of 5 ml/s. The total scan time was 54 sec and the subjects were instructed to hold their breath as long as possible, and then initiate shallow breathing.

All MRI experiments were performed on a GE Signa 3.0 T EXCITE HDx system (GE Healthcare, Waukesha, WI, USA) with gradients supporting 40 mT/m amplitude and 150 mT/m/ms slew rate. The body coil and an 8-channel cardiac array coil were used for RF transmission and signal reception, respectively. Coronary angiograms were performed using the standard techniques and tomographic images were obtained from multiple planes.

5.1.3 Data Analysis

Endocardial and epicardial borders of the left ventricle were manually drawn for each tagged and control image. For segment-based analysis, the myocardium was divided into six radial segments (anterior, anteroseptal, inferoseptal, inferior, inferolateral and anterolateral) [14], and MBF was calculated using Eq. 4.1 [12] after signal averaging in each segment. The standard deviation of the physiological noise affecting each scan was estimated using six associated measurements (one per breath-hold). Perfusion reserve was computed as $MBF_{\text{stress}}/MBF_{\text{rest}}$. To generate perfusion reserve maps, each MBF map was reconstructed with 50 radial segments, and then smoothed by convolving with a 13-point Hamming window.

CMR first-pass images and X-ray angiograms were read by two experienced cardiologists. For first-pass images, all six myocardial segments from four slices were examined

for perfusion defects. Coronary artery narrowing was visually estimated using electronic calipers. Significant stenosis was defined as $\geq 70\%$ diameter narrowing.

5.2 Results

Among the nineteen patients, the mean number of risk factors was 3.4, with 100% hypertension, 79% hypercholesterolemia, 53% age over 65, 47% diabetes mellitus, and 26% male. Eleven out of the nineteen patients were found to be “normal” based on having no visible perfusion defect on first-pass MRI, and no significant obstruction on coronary angiography (if it was performed). Five patients had CAD confirmed by X-ray angiography, comprising two patients with single-vessel disease and three patients with three-vessel disease. Three remaining patients showed perfusion defect on first-pass images but no angiographically significant stenosis.

5.2.1 Normal Subjects

Figure 5.2 contains global MBF measurements based on ASL at rest and stress from the eleven “normal” subjects. Each bar represents the average MBF across the whole myocardium in the slice. The error bars correspond to plus or minus one standard deviation of the physiological noise,

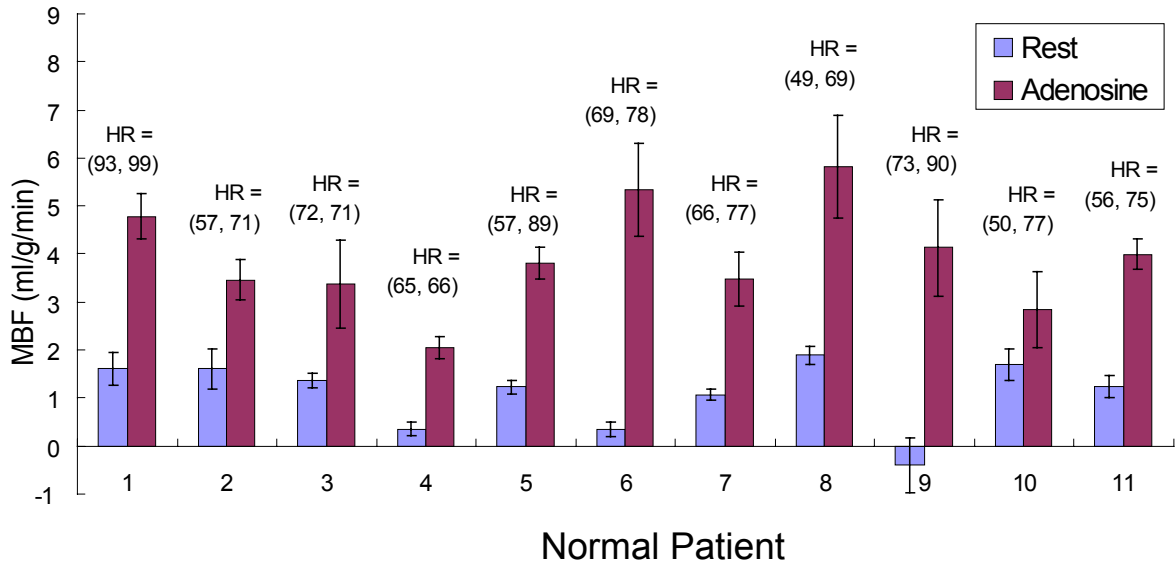


Figure 5.2. MBF estimates at rest (blue) and during adenosine infusion (purple), in eleven patients with no significant perfusion defect on first-pass imaging, and no significant disease on coronary angiography. The average MBF was 1.09 ± 0.70 ml/g/min at rest and 3.92 ± 1.08 ml/g/min with adenosine, yielding an average perfusion reserve ($MBF_{\text{stress}}/MBF_{\text{rest}}$) of 4.29. This increase in MBF was found to be statistically significant based on Student's paired t-test ($p=0.00002$). Error bars represent plus or minus one standard deviation of the measured physiological noise. The average physiological noise during adenosine infusion was 2.6 times larger than the average physiological noise at rest.

σ measured for each scan. The average MBF across subjects was 1.09 ± 0.70 ml/g/min at rest and 3.92 ± 1.08 ml/g/min during adenosine infusion, yielding an average perfusion reserve ($MBF_{\text{stress}}/MBF_{\text{rest}}$) of 4.29. Subjects with $|MBF_{\text{rest}}|/\sigma_{\text{rest}} < 2.0$ were excluded from perfusion reserve analysis because excessive noise in the denominator of the perfusion reserve equation can produce substantive errors in the estimated perfusion reserve. This resulted in exclusion of patient 9 in Figure 5.2. Based on a Student's paired t-test, the MBF increase with adenosine was found to

be statistically significant, with $p=0.00002$. The average standard deviation of physiological noise across subjects for the rest ASL scans was 0.25 ml/g/min, which is comparable to 0.21 ml/g/min measured in healthy volunteers in Ref. [108]. The average standard deviation of physiological noise for the stress ASL scans was 0.64 ml/g/min, which is roughly 2.6 times larger than that of the physiological noise at rest. The average heart rate increased by 22% from 64 bpm at rest to 78 bpm during adenosine infusion.

5.2.2 Comparison of Normal and Ischemic Segments

Table 5.1 summarizes the comparison of normal myocardial segments from the eleven normal patients and the most ischemic myocardial segments from the five patients with abnormal first-pass perfusion and angiographically significant stenosis. All six mid short-axis segments [14] were included for the normal patients. The most ischemic segments in the patients with CAD were determined by the most significant lesion on the angiograms. Segments with $|\text{MBF}_{\text{rest}}|/\sigma_{\text{rest}} < 2.0$ were excluded for the same reasons mentioned above. The average perfusion reserve was 3.00 ± 1.66 in normal segments and 1.54 ± 1.15 in ischemic segments. This difference in perfusion reserve was found to be statistically significant, with $p=0.0419$, based on a Student's unpaired t-test.

		Normal segments	Ischemic segments	
Subjects	Number of patients	11	5	
	Age	66 ± 10 yrs	62 ± 13 yrs	
	Sex	2M, 9F	2M, 3F	
	Risk factors	Hypertension	11	5
		Hypercholesterolemia	8	4
		Age over 65	6	3
		Diabetes mellitus	4	3
Male	2	2		
Segments	Number of segments included	55	6	
	Perfusion reserve ($MBF_{\text{stress}}/MBF_{\text{rest}}$)	3.00 ± 1.66*	1.54 ± 1.15*	

Table 5.1. Comparison of normal myocardial segments from the normal patients and the most ischemic myocardial segments from the patients with angiographically-significant CAD. *The difference in perfusion reserve between normal and ischemic segments was statistically significant ($p=0.0419$), based on Student's unpaired t-test.

5.2.3 Subjects with Single-vessel Disease

Figure 5.3 contains perfusion reserve maps and coronary angiograms from the two patients with single-vessel disease. Lowered perfusion reserve in the anterior wall is consistent with total occlusion of the LAD coronary artery (red arrows), and lowered perfusion reserve in the inferoseptum is consistent with total occlusion of the RCA (blue arrows). The inferior wall in the patient with LAD disease and the lateral wall in the patient with RCA disease also showed

somewhat lowered reserve, and it is not clear from the angiogram whether these reflect real perfusion deficit or merely measurement error due to high noise.

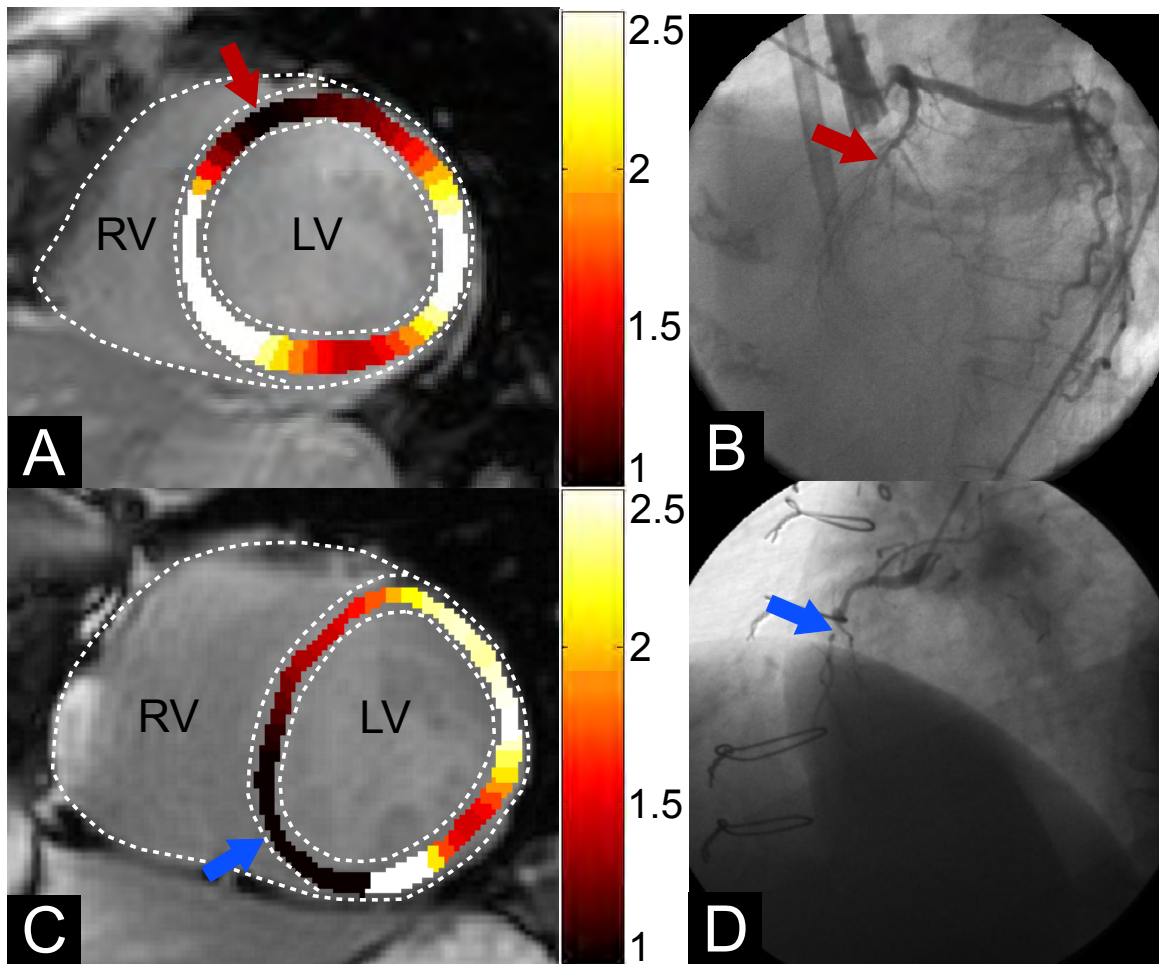


Figure 5.3. Myocardial ASL perfusion reserve maps and X-ray angiograms from the first two patients with single-vessel CAD. **A, B:** patient with total LAD occlusion, **C, D:** patient with total RCA occlusion. Myocardial regions with lowered perfusion reserve are consistent with the territories of occluded vessels (see arrows).

5.3 Discussion

In this study, we applied myocardial ASL sequences to nineteen patients scheduled for rest-stress CMR. In patients who had no visible myocardial perfusion defect on first-pass imaging and no significant obstruction on coronary angiography, we found a statistically significant increase in global MBF measurements with adenosine infusion compared to at rest. Adenosine is a widely used vasodilator that produces large increases in MBF for normal myocardium. This increase has been documented to be 4.00 ± 1.10 times based on $^{15}\text{O}\text{-H}_2\text{O}$ PET [47], which is comparable to the ASL results in this study. The present study demonstrates, for the first time, that myocardial ASL is able to detect clinically-relevant increases in MBF with vasodilatation.

This study also demonstrated the potential for rest-stress myocardial ASL to detect angiographically significant CAD. We found a statistically significant difference in measured perfusion reserve between normal myocardial segments and the most ischemic myocardial segments identified by X-ray angiography. We are in the process of accumulating a much larger cohort that spans the spectrum of CAD, from which we will be able to determine the ability of rest-stress myocardial ASL to detect angiographically significant CAD.

The current implementation of myocardial ASL suffers from greater noise and lower spatial resolution compared to state-of-the-art first-pass imaging. These are not fundamental limitations of the ASL approach, and may be resolved with technical improvements to the

imaging methodology. Even in its present form, myocardial ASL could be of value in evaluating patients with end-stage renal disease (ESRD) who are not candidates for first-pass imaging due to the risk of nephrogenic fibrosing dermopathy. There are roughly 340,000 ESRD patients in the United States [92] who require heart disease assessment every 6 to 12 months while awaiting kidney transplant, and most patients are on the wait-list for 4 to 7 years. These patients stand to benefit significantly from a new MPI approach that does not require contrast agents.

Spatial heterogeneity of MBF is typically represented by relative dispersion (RD, $SD/mean$) and has been observed in humans and animals [15, 21, 43, 50, 60]. It was reported to be 0.13 with 4 segments of myocardium (anterior, lateral, septal, and inferior walls) using PET in humans [15], and 0.26 with 8 segments of myocardium using microspheres in baboons [50]. RD from our eleven normal patients was found to be 0.84 with 6 myocardial segments, implying relatively high noise in our measurements. The intrinsic spatial heterogeneity of MBF may be attributed to different metabolic needs, oxygen demand, and neural regulatory modification in different regions [21, 43, 60]. Transit delay in ASL techniques can also introduce methodological spatial heterogeneity depending on vascular geometry.

We examined the spatial correlation of physiological noise in our nineteen patients. Figure 5.4 shows standard deviation of physiological noise as a function of ROI size, averaged across the subjects in resting scans. If physiological noise was not spatially correlated at all, the standard deviation should be inversely proportional to the square root of ROI size. This plot is

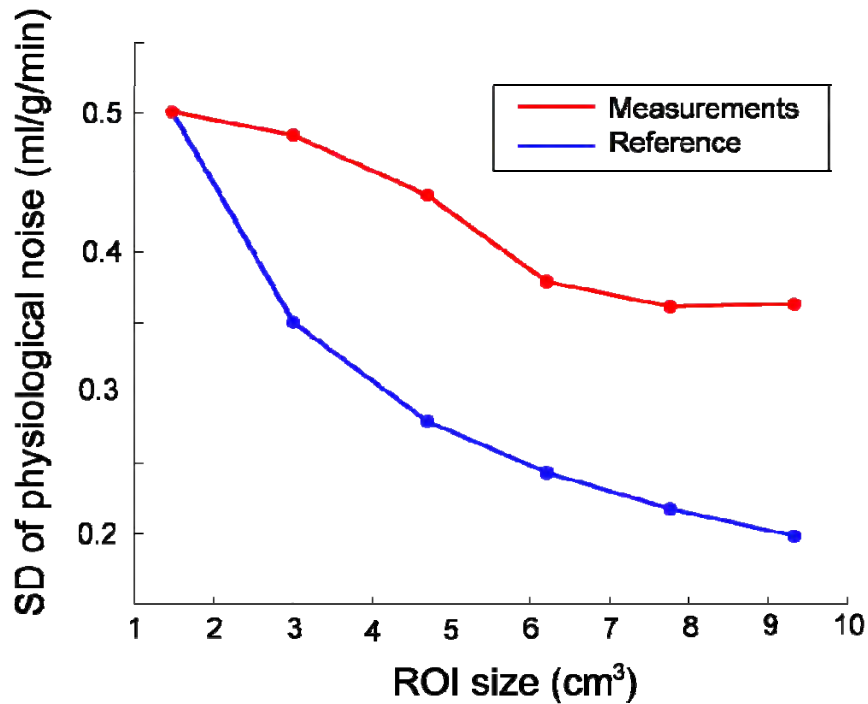


Figure 5.4. Standard deviation of physiological noise as a function of ROI size, averaged across 19 patients in resting scans. If physiological noise was not spatially correlated at all, the standard deviation should be inversely proportional to the square root of ROI size (as indicated by “Reference”).

denoted by “Reference” in Figure 5.4. The discrepancy between measured physiological noise and “Reference” demonstrates spatial correlation in physiological noise.

In this work, we invoked the widely-used kinetic model [12] to convert ASL signal amplitudes to MBF estimates. While it is known that ASL signal amplitude is proportional to tissue blood flow, there are other factors that may influence the quantitative accuracy of the approach. One natural follow-up to this study would be to compare ASL estimates of MBF against an independent gold-standard, such as quantitative PET, in humans.

Myocardial ASL is also limited by SNR, and requires signal averaging spatially and over multiple repetitions to generate meaningful data. We previously found that physiological noise (which includes all variations over time) is the critical factor that determines the sensitivity to MBF [108]. Patient 9 (see Figure 5.2), represents the worst case from the present study, which suffered from physiological noise three times higher than the average across subjects, and resulted in a negative resting MBF measurement. Sources of physiological noise may include metabolic fluctuation, respiratory and cardiac motion, and subject discomfort. The fact that physiological noise was 2.6 times larger during adenosine infusion suggests that subject motion or discomfort may be a significant source. We are currently investigating several potential sources of physiological noise and are evaluating solutions that involve improved pulse sequence.

Chapter 6

Attempts to Reduce Physiological Noise

Myocardial perfusion imaging using ASL shows promise but produces high physiological noise. High physiological noise reduces the measurement confidence, and thus delays its transition to clinical use. We determined that physiological noise reduction is critical to improving the robustness of myocardial ASL, and explored three different approaches to reduce physiological noise. In this chapter, we describe the hypothesis, method, and results with each attempt.

One potential source of the physiological noise we suspected was the error caused by static tissue mis-registration between control and tagged images. To reduce this error, we utilized background suppression (BGS) which has been widely used in brain ASL as a means to reduce such physiological noise [110].

Another potential source of physiological noise was the large apparent ASL signal in the blood pool due to inadvertent tagging of blood in the LA and/or LV. A high blood pool signal adjacent to myocardium may interfere with MBF measurements because of partial voluming and k-space truncation, and therefore we hypothesized that the irregular variation of blood pool signal

caused the variation in myocardial ASL signal [108]. We applied a new pulsed tagging method using a 2D spatially selective adiabatic inversion of the proximal aorta, and compared the results with those using conventional 1D spatially selective tagging [111].

Lastly, we considered any variation during each breath-hold as a source of physiological noise. We used pre-saturation of the imaging volume and reduced the duration of each breath-hold from 10-11 second to 3-4 second [59]. To achieve saturation residue negligible enough for myocardial ASL, we implemented B_1 -insensitive pre-saturation of myocardium using weighted sub-pulses that were optimized for measured B_1 variation [90].

6.1 Myocardial Background Suppression

6.1.1 Methods

We incorporated BGS pulse into our FAIR-SSFP sequence as illustrated in Figure 6.1. BGS pulse comprised one slab-selective saturation pulse and one nonselective inversion pulse. The timing of this inversion pulse was adjusted in real-time to achieve myocardial BGS at the imaging time regardless of heart rate. Experiments were performed on a 3 T scanner (Signa EXCITE, GE) with an 8-channel cardiac array coil. Regions of septal myocardium on mid-short axis were manually segmented for each breath-hold. MBF was estimated using Buxton's general kinetic model [12].

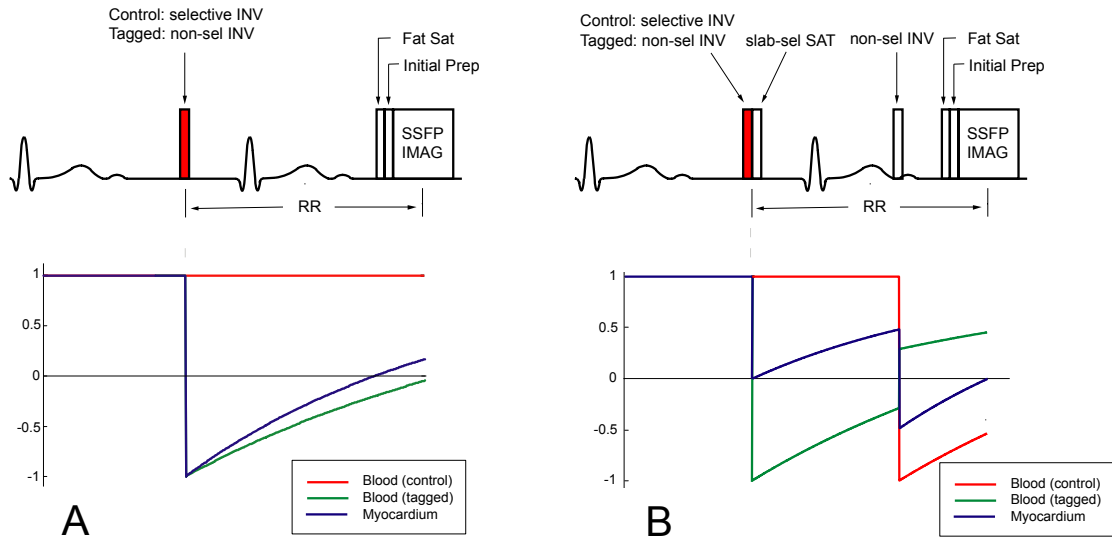


Figure 6.1. Cardiac gated FAIR – SSFP pulse sequences **A:** without and **B:** with myocardial BGS.

The standard deviation of the physiological noise was calculated based on measurements from six breath-holds with an assumption of Gaussian model.

6.1.2 Results

Table 6.1 summarizes the results from all ten scans. Using BGS, the myocardial tissue signal was reduced from 32% to 6% (yellow columns), MBF estimates decreased by 44%, and standard deviation of the physiological noise increased slightly (blue columns). Using a paired t-tests, the

Scan	FAIR			FAIR with BGS		
	Myo. signal (%)	MBF	SD of p. noise	Myo. signal (%)	MBF	SD of p. noise
1	27	0.84	0.278	3	0.79	0.290
2	31	0.97	0.145	6	0.61	0.286
3	52	0.67	0.052	12	0.26	0.167
4	43	0.85	0.104	5	0.33	0.191
5	41	0.98	0.181	6	0.29	0.036
6	32	0.66	0.055	4	0.14	0.092
7	34	0.78	0.155	5	0.33	0.245
8	23	0.66	0.133	4	0.67	0.124
9	38	1.02	0.087	9	0.69	0.095
10	22	1.04	0.136	5	0.65	0.110
Avg.	32	0.85	0.133	6	0.47	0.164

Table 6.1. Average myocardial signal on control and tagged images with respect to equilibrium signal, MBF estimate (in ml/g/min), and standard deviation of physiological noise (in ml/g/min).

decrease in measured MBF was found to be statistically significant ($p=0.0004$) while the change in standard deviation of the physiological noise was found to be statistically insignificant ($p=0.2697$).

6.1.3 Discussion

While cardiac-gated FAIR tagging methods already have relatively low myocardial signal in control and tagged images due to inversion of imaging volume, myocardial BGS pulses were able

to reduce this further by 82%. Results from ten scans show that myocardial BGS produced no significant change in physiological noise, which suggests that static tissue mis-registration in the subtraction is not a significant source of physiological noise in human myocardial ASL. However, this only implies that incomplete subtraction of myocardial signal is not a dominant source. Blood pool signal is not affected by BGS pulses, and the signal leakage from blood pool to myocardium, if any, can be mis-matched due to control/tagged image mis-registration, leading to high physiological noise and measurement errors. Blood pool signal as a potential source of noise is discussed in the next section. Despite insignificant change in physiological noise, measured MBF was significantly lower with myocardial BGS. This may be due to the long saturation duration (20ms) or corruption of saturation caused by preceding inversion pulse. This remains to be determined.

6.2 Blood Pool Signal Suppression Using Pulsed 2D Tagging

6.2.1 Methods

Our approach used 2D selective inversion pulses oriented perpendicular to a standard three-chamber view, tagging blood in the proximal aorta while leaving the LA and LV undisturbed. We utilized the strategy of Conolly et al [17] to design 2D spatially selective adiabatic inversion

pulses, and further reduced the pulse duration and peak B_1 using the VERSE transform [16]. Figure 6.2 shows our design of RF pulse and associated gradients. The composite pulse used 24 subpulses, each a small tip SLR pulse [72] with a time-bandwidth product of 3 and a duration of 0.5 ms prior to VERSE transformation. The overall sech envelope [88] had shape parameters $\mu = 2.5$ and $b = 800$. The gradient waveform used a flyback EPI trajectory for insensitivity to flow effects and timing errors. The overall duration of the pulse was 23 ms, which is short compared to the T_2 of arterial blood at 3 T (approx. 141 ms) [7].

The cardiac gated pulse sequence is illustrated in Figure 6.3. Pulsed inversion occurs immediately after the aortic valve closes, and imaging is centered at mid-diastole in the following heartbeat. The timing of both were determined by a CINE scout scan. Imaging protocol was the same as in FAIR-SSFP sequence. Each pair of control and tagged images was acquired 6 s apart during a single breath-hold, and six breath-holds (10-12 sec each) were performed for signal averaging. Image acquisition was performed using a snapshot 2DFT balanced SSFP sequence with 3.2 ms TR and 50° flip angle. Experiments were performed in 7 healthy volunteers on a 3 T scanner (Signa EXCITE, GE) with an 8-channel cardiac array coil. For a comparison, conventional pulsed ASL using 1D adiabatic inversion was performed as well in the same subjects with the same imaging parameters.

Regions of septal myocardium were manually segmented for each breath-hold. We assumed that the 2D inversion tags all the blood at the root of the aorta that will travel into the coronaries during the following diastole, and hence used the equation

$$MBF = \frac{C - T}{2\alpha \cdot C \cdot RR \cdot e^{-T_i/T_1} \cdot \rho} \quad (6.1)$$

derived from Buxton's general kinetic model [12] to arrive at the average perfusion rate over one R-R interval, where C , T , α , RR , T_i , and T_1 refer to the mean myocardial signal in the control and tagged images, inversion efficiency, R-R interval, inversion time, and T_1 of blood, respectively.

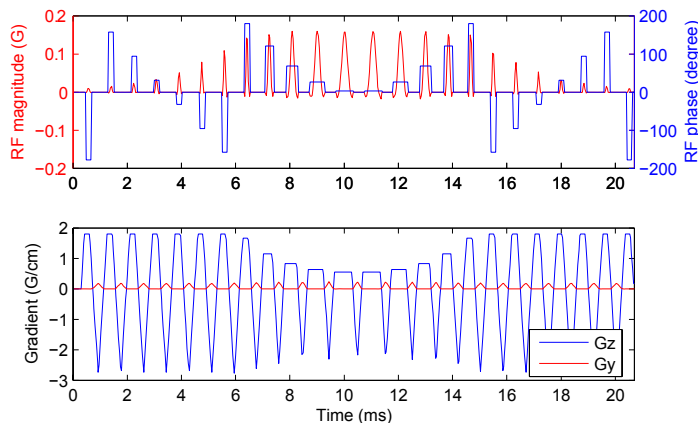


Figure 6.2. 2D selective adiabatic inversion pulse. (23 ms duration, 0.16 G peak B_1+).

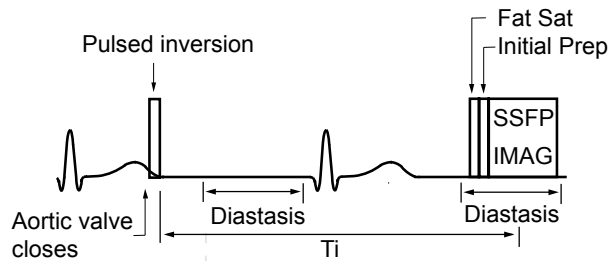


Figure 6.3. Cardiac gated "pulsed" myocardial ASL sequence.

6.2.2 Results

Figure 6.4 illustrates in-vivo 1D and 2D tag profiles and corresponding ASL difference images for one representative subject. Tag profiles were measured by dividing two snapshot images (2DFT gradient echo, center-out view order); images with and without inversion pulse immediately prior to imaging. Table 6.2 contains the results from all subjects. The average inversion efficiency of 2D tagging was 92%, which was comparable to 93% with 1D tagging. The residual LV signal was reduced from 50% to 5% using 2D tagging. We estimated MBF and the standard deviation of the physiological noise based on Gaussian model. Using 2D tagging, standard deviation of the physiological noise decreased by 44% and this difference was found to be statistically significant based on paired t-test with $p = 0.0476$. MBF measurements were also found to be reduced by 66% with 2D tagging.

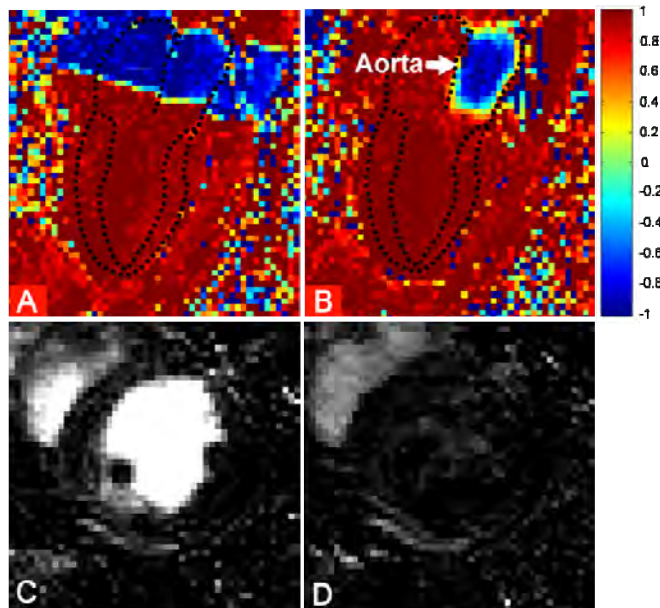


Figure 6.4. In-vivo tag profiles for A: 1D tagging and B: 2D tagging of the proximal aorta. Identically windowed difference images for C: 1D tagging and D: 2D tagging.

scan	1D tagging				2D tagging			
	Inv. effi.	LV signal	MBF	SD of p. noise	Inv. effi.	LV signal	MBF	SD of p. noise
1	96%	84%	1.87	0.404	92%	2%	0.59	0.147
2	91%	31%	0.36	0.125	94%	4%	0.13	0.094
3	99%	36%	1.64	0.162	98%	2%	0.43	0.117
4	97%	33%	0.83	0.164	94%	5%	0.11	0.045
5	93%	47%	1.35	0.174	92%	8%	0.82	0.129
6	88%	69%	1.89	0.138	82%	8%	0.63	0.156
7	87%	48%	1.65	0.175	94%	9%	0.58	0.066
Avg.	93%	50%	1.37	0.192	92%	5%	0.47	0.108

Table 6.2. Inversion efficiency across the proximal aorta, residual LV signal ((C-T)/C on LV blood), MBF measurements (in ml/g/min), and SD of physiological noise (in ml/g/min) for 1D and 2D tagging schemes.

6.2.3 Discussion

In this study, 2D spatially selective adiabatic inversion pulses were used to efficiently tag blood in the proximal aorta while leaving the LA and LV unperturbed. These pulses achieved inversion efficiency comparable to that of 1D inversion, and reduced the physiological noise in the resulting MBF measurements, suggesting that the spurious blood pool signal is an important source of physiological noise in myocardial ASL. Reduced MBF estimates may reflect the possibility that high blood pool signal with 1D tagging may result in overestimated MBF. This

remains to be determined. Unlike FAIR tagging, this method requires extra effort to localize proximal aorta and place a relevant size of tag onto it. The direction of tagging block should also be carefully determined because the 2D selective inversion pulse creates replicas along one direction and these can perturb the upstream blood in LA or lung. The performance of these steps may vary for different operators but is critical for accurate measurements.

6.3 Breath-hold Duration Reduction Using Pre-saturation

6.3.1 Methods and Results

Pulse Sequence: Myocardial ASL was performed using FAIR-SSFP as described in Chapter 4. FAIR with an extra RF pulse (FAIRER) [59] was implemented by adding slab-selective saturation immediately after the inversion pulse, as shown in Figure 6.5. Each ASL scan consisted of six breath-holds, with one pair of control and tagged images acquired in each breath-hold. Experiments were performed on a GE Signa 3.0 T EXCITE using a custom pulse sequence, and 8-channel cardiac array coil.

Saturation Pulse: B_1 -insensitive saturation was achieved using a tailored pulse train [90], optimized to minimize $\max|M_z/M_0|$ at the end of the pulse. Each sub-pulse was a sinc with

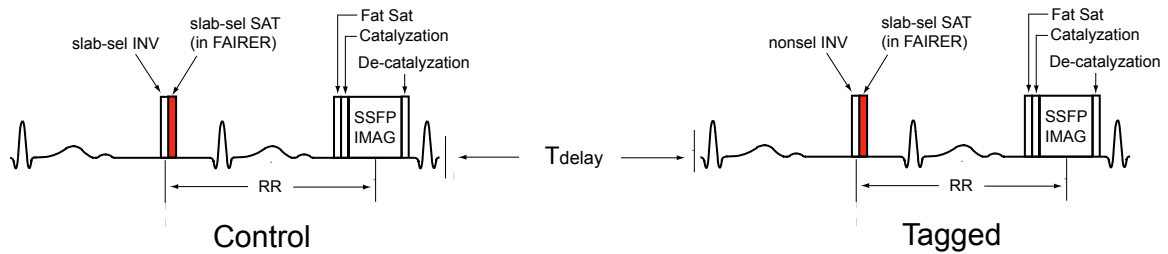


Figure 6.5. Myocardial ASL pulse sequence of FAIR or FAIRER in each breath-hold. Control and tagged imaging are separated by T_{delay} .

TBW=4 followed by a crusher gradient. The prescribed sub-pulse flip angles of 167° -- 173° -- 121° -- 119° -- 102° were optimized for B_1 scale = 0.5 to 0.9 with pulse duration of 21 ms.

Required Delay Between Control and Tagged Images: MBF error due to imperfect static tissue subtraction was measured by acquiring two control images in each breath-hold (see Figure 6.6). With FAIR, the measured MBF error increased as T_{delay} decreased because of incomplete relaxation of static tissue, and there was an excellent agreement with simulation. MBF error with FAIRER was relatively independent of T_{delay} and the average error was 0.09 ml/g/min, which supports the use of pre-saturation to reduce breath-hold duration.

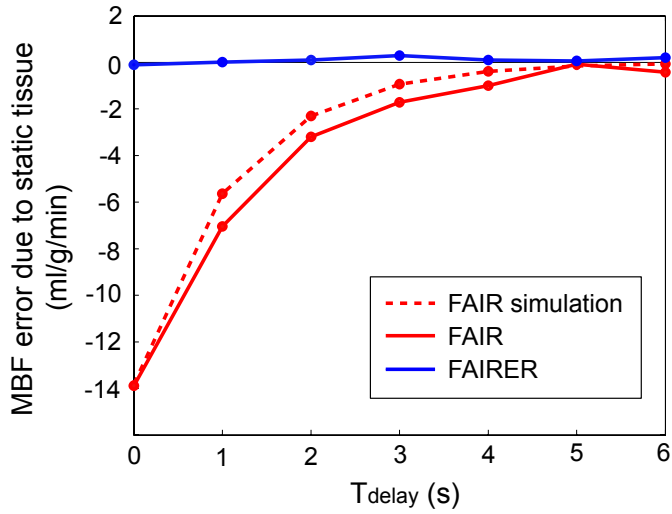


Figure 6.6. MBF error due to imperfect static tissue subtraction as a function of time delay between control and tagged imaging.

Scan	FAIR		FAIRER	
	MBF	SD of p. noise	MBF	SD of p. noise
1	1.19	0.088	0.27	0.052
2	1.09	0.058	0.75	0.089
3	0.22	0.207	0.04	0.124
4	0.75	0.024	0.46	0.086
5	0.70	0.236	-0.06	0.061
6	-0.09	0.122	0.16	0.278
7	0.44	0.043	0.04	0.175
Avg.	0.61	0.111	0.24	0.124

Table 6.3. MBF measurements and SD of physiological noise using FAIR with $T_{\text{delay}} = 6$ sec and FAIRER with $T_{\text{delay}} = 0$ sec (in ml/g/min).

MBF Measurements: MBF measurements were performed using FAIR with $T_{\text{delay}} = 6$ s and FAIRER with $T_{\text{delay}} = 0$ s in four healthy volunteers (see Table 6.3). The average MBF was 0.61 ± 0.46 ml/g/min with FAIR and 0.24 ± 0.28 ml/g/min with FAIRER. This difference in physiological noise was found to be statistically insignificant with $p = 0.7908$ based on paired t-test.

6.3.2 Discussion

Shortening the breath-hold duration has potential to reduce unknown temporal variation during each breath-hold. Using an extra RF saturation pulse, we were able to shorten the duration of breath-hold from 10-11 sec to 3-4 sec without introducing measurement error. While the difference in physiological noise with pre-saturation was statistically insignificant, it may be effective at physiological noise reduction in patients who have difficulty with long breath-holds. We also noticed a significant difference in the ASL signal between FAIR and FAIRER acquisitions. One possible explanation is that with FAIR, blood that enters the slice prior to inversion may be in different states in the control and tagged images, while in FAIRER, the saturation pulse resets the history of imaging slice and the MBF measurement only reflects the blood flow that arrives in the imaging slice after inversion. This remains to be verified.

Chapter 7

Summary and Future Work

7.1 Summary

This dissertation demonstrates application of ASL in myocardial perfusion imaging at 3T. Because ASL is more challenging in the heart compared to other stationary tissues, it is important to utilize more simple and robust ASL tagging technique but with highly SNR-efficient imaging sequence. Using the proposed sequence, we have demonstrated that myocardial ASL is feasible and has potential to detect angiographically significant CAD with vasodilatation. We have also presented analysis of measurement error with respect to thermal and physiological noise to provide guidance to what extent that MBF can be measured accurately with a certain confidence, and to demonstrate that physiological noise should be reduced down to thermal noise level. For physiological noise reduction, we have attempted several methods and obtained promising results with 2D spatially selective tagging.

7.2 Future Work

7.2.1 Extended Spatial Coverage

In perfusion imaging, a large spatial coverage is required for accurate estimation of MBF and its prognostic value. While we have not utilized acceleration techniques due to SNR loss in these methods, acceleration can be used to increase the spatial coverage not to reduce the scan time. For example, the current protocol with single slice imaging can be extended directly to two slices using two-fold acceleration with SENSE [76] or GRAPPA [33] without loss of SNR. In this case, two-separate-slice excitation using a cosine-modulated sinc RF pulse will be desired to increase the diagnostic efficiency. Compressed sensing [57] combined with conventional acceleration techniques can also be considered to increase the acceleration. 3D imaging, while requiring higher acceleration, will provide higher coil sensitivity which can be utilized in acceleration methods.

7.2.2 Systolic Imaging

MR image acquisition is typically performed at mid-diastole, which is the longest stationary cardiac phase. End-systole is the second longest quiescent phase and is suited for MR image acquisition [29, 85]. It is known to have timing and duration less sensitive to irregular heartbeat. Myocardial ASL with systolic imaging may reduce physiological noise by minimizing mismatch between control and tagged images due to gating error. In addition, systolic images will obtain more number of voxels averaged to suppress thermal noise, and facilitate the detection of non-transmural perfusion defects. The biggest hurdle for systolic imaging is the short duration, and this requires the use of acceleration techniques. While acceleration reduces SNR, increased number of voxels averaged and minimized control-tagged mismatch may, in turn, lower the physiological noise.

7.2.3 Other Tagging Methods

All the previous works on myocardial ASL including ours used FAIR tagging mainly because FAIR is among the most robust tagging method. However, myocardial ASL may adopt other tagging schemes such as velocity selective tagging [100] or pseudocontinuous tagging [18, 101] that have been well received in brain ASL recently. In velocity selective ASL, tagging is achieved

based on the velocity of arterial blood spins, not based on the spatial location. Therefore this technique reduces the error due to transit delay of tagged blood. Patients with significant collateral flow to the myocardium will benefit this tagging method. On the other hand, pseudocontinuous tagging can in principle provide the highest tagging efficiency with roughly two-fold ASL signal compared to conventional tagging schemes. Myocardial ASL with pseudocontinuous tagging can achieve doubled SNR but may increase physiological noise due to irregular pattern of pulsatile blood flow. Spatial and temporal position of inversion plane should be carefully determined considering arterial blood path in coronaries and pulsatile flow pattern to maximize tagging efficiency.

7.2.4 Cross-validation with Other Modalities

Myocardial ASL should be compared with other modalities such as PET or microsphere methods to evaluate quantitation. While there have been quantitation issues with PET, microsphere method applied in animals is a well-established gold standard in myocardial perfusion imaging. Human-sized animals with and without pathology would be suited for comparison with microspheres. For accurate comparison, all the modeling assumption in myocardial ASL should be examined. For example, if transit delay is found to be critical in myocardial ASL, application of techniques less sensitive to this such as QUIPSS II [99] may be considered. Note that because the scan sessions

for ASL and other modalities can be on different days, comparison will require the same condition in subjects for both sessions such as no caffeine/food intake prior to scans.

References

- [1] M. F. Allard, C. T. Kamimura, S. L. Henning, and B. R. Wiggs, "Regional myocardial capillary erythrocyte transit time in the normal resting heart," *Circulation Research*, vol. 72, pp. 187–193, 1993.
- [2] J. An, A. Voorhees, and Q. Chen, "SSFP Arterial Spin Labeling Myocardial Perfusion Imaging at 3 Tesla," *In: Proceedings of the 13th Annual Meeting of ISMRM, Miami Beach, FL, USA*, p. (Abstract 253), 2005.
- [3] A. A. Barmeyer, A. Stork, K. Muellerleile, C. Tiburtius, A. K. Schofer, T. A. Heitzer, T. Hofmann, G. Adam, T. Meinertz, and G. K. Lund, "Contrast-enhanced cardiac MR imaging in the detection of reduced coronary flow velocity reserve," *Radiology*, vol. 243, pp. 377 - 385, 2007.
- [4] W. R. Bauer, F. Roder, K. H. Hiller, H. Han, S. Frohlich, E. Rommel, A. Haase, and G. Ertl, "The effect of perfusion on T1 after slice-selective spin inversion in the isolated cardioplegic rat heart: measurement of a lower bound of intracapillary-extravascular water proton exchange rate," *Magn Reson Med*, vol. 38, pp. 917–923, 1997.
- [5] S. R. Bergmann, K. A. Fox, K. D. McElvany, M. J. Welch, J. Markham, and B. E. Sobel, "Quantification of regional myocardial blood flow in vivo with H₂¹⁵O," *Circulation*, vol. 70, pp. 724 - 733, 1984.
- [6] M. A. Bernstein, K. F. King, and X. J. Zhou, "Handbook of MRI pulse sequences " 2004.
- [7] X. Bi, V. Deshpande, O. Simonetti, G. Laub, and D. Li, "Three-Dimensional Breathhold SSFP Coronary MRA: A Comparison Between 1.5T and 3.0T," *J Magn Reson Imaging*, vol. 22, pp. 206 - 212, 2005.
- [8] F. Bloch, "Nuclear Induction," *Physics Review* vol. 70, pp. 460-473, 1946.

- [9] U. Blume, M. Guenther, A. Chiribiri, S. Plein, and T. Schaeffter, "Qualitative and quantitative myocardial perfusion with arterial spin labeling," *In: Proceedings of the 17th Annual Meeting of ISMRM, Honolulu*, 2009.
- [10] D. S. Bolar, D. L. Levin, S. R. Hopkins, L. F. Frank, T. T. Liu, E. C. Wong, and R. B. Buxton, "Quantification of Regional Pulmonary Blood Flow Using ASL-FAIRER," *Magn Reson Med*, vol. 55, pp. 1308 - 1317, 2006.
- [11] R. B. Buxton, C. R. Fisel, D. Chien, and T. J. Brady, "Signal intensity in fast NMR imaging with short repetition times," *J Magn Reson*, vol. 83, pp. 576–585, 1989.
- [12] R. B. Buxton, L. R. Frank, E. C. Wong, B. Siewert, S. Warach, and R. R. Edelman, "A general kinetic model for quantitative perfusion imaging with arterial spin labeling," *Magn Reson Med*, vol. 40, pp. 383–396, 1998.
- [13] H. Y. Carr, "Steady-state free precession in nuclear magnetic resonance," *Physical Review*, vol. 112, pp. 1693-1701, 1958.
- [14] M. D. Cerqueira, N. J. Weissman, V. Dilsizian, A. K. Jacobs, S. Kaul, W. K. Laskey, D. J. Pennell, J. A. Rumberger, T. Ryan, and M. S. Verani, "Standardized myocardial segmentation and nomenclature for tomographic imaging of the heart: a statement for healthcare professionals from the cardiac imaging committee of the council on clinical cardiology of the American Heart Association," *Circulation Research*, vol. 105, pp. 539–542, 2002.
- [15] P. Chareonthaitawee, P. A. Kaufmann, O. Rimoldi, and P. G. Camici, "Heterogeneity of resting and hyperemic myocardial blood flow in healthy humans.," *Cardiovasc Res*, vol. 50, pp. 151–161, 2001.
- [16] S. Conolly, D. Nishimura, A. Macovski, and G. Glover, "Variable-rate selective excitation," *J Magn Reson* vol. 78, pp. 440–458, 1988.
- [17] S. Conolly, J. Pauly, D. Nishimura, and A. Macovski, "Two-dimensional selective adiabatic pulses," *Magn Reson Med*, vol. 24, pp. 302–313, 1992.
- [18] W. Dai, D. Garcia, C. d. Bazelaire, and D. C. Alsop, "Continuous Flow-Driven Inversion for Arterial Spin Labeling Using Pulsed Radio Frequency and Gradient Fields," *Magn Reson Med*, vol. 60, pp. 1488-1497, 2008.

- [19] M. Deimling and O. Heid, "Magnetization prepared true FISP imaging," *In: Proc Second Annual Meeting of the Society of Magnetic Resonance, San Francisco*, p. 495, 1994.
- [20] J. A. Detre, J. Wang, Z. Wang, and H. Rao, "Arterial spin-labeled perfusion MRI in basic and clinical neuroscience," *Curr Opin Neurol*, vol. 22, pp. 348-55, 2009.
- [21] A. Deussen, "Blood flow heterogeneity in the heart," *Basic Res Cardiol*, vol. 93, pp. 430–438, 1998.
- [22] R. Dharmakumar and G. A. Wright, "Understanding steady-state free precession: a geometric perspective," *Concepts Magn. Reson. A*, vol. 26, pp. 1-10, 2005.
- [23] E. V. R. Di Bella, D. L. Parker, and A. J. Sinusas, "On the dark rim artifact in dynamic contrast-enhanced MRI myocardial perfusion studies," *Magn Reson Med*, vol. 54, pp. 1295-1299, 2005.
- [24] J. H. Duyn, C. X. Tan, P. van Gelderen, and M. N. Yongbi, "High-sensitivity singleshot perfusion-weighted fMRI," *Magn Reson Med*, vol. 46, pp. 88–94., 2001.
- [25] M. Fenchel, P. Martirosian, J. Langanke, J. Giersch, S. Miller, N. I. Stauder, U. Kramer, C. D. Claussen, and F. Schick, "Perfusion MR imaging with FAIR true FISP spin labeling in patients with and without renal artery stenosis: initial experience," *Radiology*, vol. 238, pp. 1013-21, 2006.
- [26] R. Freeman and H. D. W. Hill, "Phase and intensity anomalies in Fourier transform NMR," *J Magn Reson*, vol. 4, pp. 366–383, 1971.
- [27] D. M. Garcia, G. Duhamel, and D. C. Alsop, "Efficiency of inversion pulses for background suppressed arterial spin labeling," *Magn Reson Med*, vol. 54, pp. 366–372, 2005.
- [28] M. Garwood and Y. Ke, "Symmetric pulses to induce arbitrary flip angles with compensation for RF inhomogeneity and resonance offsets," *J Magn Reson*, vol. 94, pp. 511–525, 1991.
- [29] A. M. Gharib, D. A. Herzka, A. O. Ustun, M. Y. Desai, J. Locklin, R. I. Pettigrew, and M. Stuber, "Coronary MR angiography at 3T during diastole and systole," *J Magn Reson Imaging*, vol. 26, pp. 921–926, 2007.

- [30] K. L. Gould and K. Lipscomb, "Effects on coronary stenoses on coronary flow reserve and resistance," *Am J Cardiol*, vol. 34, pp. 48–55, 1974.
- [31] K. L. Gould, K. Lipscomb, and G. W. Hamilton, "Physiologic basis for assessing critical coronary stenosis. Instantaneous flow response and regional distribution during coronary hyperemia as measures of coronary flow reserve," *Am J Cardiol*, vol. 33, pp. 87-94, 1974
- [32] M. J. Graves, D. Emmens, H. Lejay, H. Hariharan, J. Polzin, and D. J. Lomas, "T2 and T2* quantification using optimal B1 image reconstruction for multicoil arrays," *J Magn Reson Imaging* vol. 28, pp. 278–281, 2008.
- [33] M. A. Griswold, P. M. Jakob, R. M. Heidemann, M. Nittka, V. Jellus, J. Wang, B. Kiefer, and A. Haase, "Generalized autocalibrating partially parallel acquisitions (GRAPPA)," *Magn Reson Med*, vol. 47, 2002.
- [34] C. J. Hardy, W. A. Edelstein, and D. Vatis, "Efficient adiabatic fast passage for NMR population-inversion in the presence of radiofrequency field inhomogeneity and frequency offsets," *J Magn Reson*, vol. 66, pp. 470 - 482, 1986.
- [35] C. J. Hardy, H. E. Cline, R. O. Giaquinto, T. Niendorf, A. K. Grant, and D. K. Sodickson, "32-element receiver-coil array for cardiac imaging," *Magn Reson Med* vol. 55, pp. 1142–1149, 2006.
- [36] B. A. Hargreaves, S. S. Vasanawala, J. M. Pauly, and D. G. Nishimura, "Characterization and reduction of the transient response in steady-state MR imaging," *Magn Reson Med*, vol. 46, pp. 49–158, 2001.
- [37] B. A. Hargreaves, G. E. Gold, C. F. Beaulieu, S. S. Vasanawala, D. G. Nishimura, and J. M. Pauly, "Comparison of new sequences for high-resolution cartilage imaging," *Magn Reson Med*, vol. 49, pp. 700-709, 2003.
- [38] "Heart Disease and Stroke Statistics – 2010 update," *American Heart Association*, 2010.
- [39] R. H. Helfant, M. A. De Villa, and S. G. Meister, "Effect of sustained isometric handgrip exercise on left ventricular performance," *Circulation*, vol. 44, pp. 982–993, 1971.
- [40] J. Hennig, O. Speck, and K. Scheffler, "Optimization of signal behavior in the transition to driven equilibrium in steady-state free precession sequences," *Magn Reson Med*, vol. 48, pp. 801-809, 2002.

- [41] T. Higuchi and F. M. Bengel, "Cardiovascular nuclear imaging: from perfusion to molecular function," *Heart* vol. 94, pp. 809-816, 2008.
- [42] W. S. Hinshaw, "Image formation by nuclear magnetic resonance: the sensitive-point method," *J Appl Phys* vol. 8, pp. 3709-3721, 1976.
- [43] J. I. E. Hoffman, "Heterogeneity of myocardial blood flow " *Basic Res Cardiol*, vol. 90, pp. 103 - 111, 1995.
- [44] M. Ibaraki, S. Miura, E. Shimosegawa, S. Sugawara, T. Mizuta, A. Ishikawa, and M. Amano, "Quantification of cerebral blood flow and oxygen metabolism with 3-dimensional PET and 15O: validation by comparison with 2-dimensional PET," *J Nucl Med* vol. 49, pp. 50-59, 2008.
- [45] E. T. Jaynes, "Matrix treatment of nuclear induction," *Physical Review*, vol. 98, pp. 1099–1105, 1955.
- [46] M. Jerosch-Herold, R. T. Seethamraju, C. M. Swingen, N. M. Wilke, and A. E. Stillman, "Analysis of myocardial perfusion MRI," *J. Magn. Reson. Imaging*, vol. 19, pp. 758–770, 2004.
- [47] P. A. Kaufmann, O. E. Rimoldi, T. Gneccchi-Ruscione, T. F. Luscher, and P. G. Camici, "Systemic nitric oxide synthase inhibition improves coronary flow reserve to adenosine in patients with significant stenoses," *Am J Physiol Heart Circ Physiol*, vol. 293, pp. H2178-82, 2007.
- [48] C. Kiefer, G. Schroth, J. Gralla, N. Diehm, I. Baumgartner, and M. Husmann, "A feasibility study on model-based evaluation of kidney perfusion measured by means of FAIR prepared true-FISP arterial spin labeling (ASL) on a 3-T MR scanner," *Acad Radiol*, vol. 16, pp. 79-87, 2009
- [49] S.-G. Kim, "Quantification of regional cerebral blood flow change by flow-sensitive alternating inversion recovery (FAIR) technique: application to functional mapping.," *Magn Reson Med*, vol. 34, pp. 293–301, 1995.
- [50] R. King, J. Bassingthwaighe, J. Hales, and L. Rowell, "Stability of heterogeneity of myocardial blood flow in normal awake baboons," *Circ. Res.*, vol. 57, pp. 285-295, 1985.

- [51] C. Kivowitz, W. W. Parmley, R. Donoso, H. Marcus, W. Ganz, and H. J. Swan, "Effects of isometric exercise on cardiac performance. The grip test.," *Circulation*, vol. 44, pp. 994–1002, 1971.
- [52] F. Kober, I. Iltis, P. J. Cozzone, and M. Bernard, "Myocardial blood flow mapping in mice using high-resolution spin labeling magnetic resonance imaging: influence of ketamine/xylazine and isoflurane anesthesia," *Magn Reson Med*, vol. 53, pp. 601–606, 2005.
- [53] K. K. Kwong, D. A. Chesler, R. M. Weisskoff, K. M. Donahue, T. L. Davis, L. Ostergaard, T. A. Campbell, and B. R. Rosen, "MR perfusion studies with T1-weighted echo planar imaging," *Magn Reson Med*, vol. 34, pp. 878–887, 1995.
- [54] A. Lafaneche`re, F. Pe`ne, C. Goulenok, A. Delahaye, V. Mallet, G. Choukroun, J. D. Chiche, J. P. Mira, and A. Cariou, "Changes in aortic blood flow induced by passive leg raising predict fluid responsiveness in critically ill patients," *Crit Care*, vol. 10, 2006.
- [55] P. Le Roux, "Simplified model and stabilization of SSFP sequences," *J Magn Reson*, vol. 163, pp. 23-37, 2003
- [56] D. K. Lowe, D. A. Rothbaum, P. L. McHenry, B. C. Corya, and S. B. Knoebel, "Myocardial blood flow response to isometric (handgrip) and treadmill exercise in coronary artery disease. ," *Circulation*, vol. 51, pp. 126–131, 1975.
- [57] M. Lustig, D. L. Donoho, and J. M. Pauly, "Sparse MRI: The Application of Compressed Sensing for Rapid MR Imaging," *Magn Reson Med*, vol. 58, pp. 1182 - 1195, 2007.
- [58] O. M. Mühling, M. E. Dickson, A. Zenovich, Y. Huang, B. V. Wilson, R. F. Wilson, I. S. Anand, R. T. Seethamraju, M. Jerosch-Herold, and N. M. Wilke, "Quantitative magnetic resonance first-pass perfusion analysis: inter- and intraobserver agreement.," *J Cardiovasc Magn Reson.*, vol. 3, pp. 247-256, 2001.
- [59] V. M. Mai and S. S. Berr, "MR perfusion imaging of pulmonary parenchyma using pulsed arterial spin labeling techniques: FAIRER and FAIR.," *J Magn Reson Imaging*, vol. 9, pp. 483-487. , 1999.
- [60] M. L. Marcus, R. E. Kerber, J. C. Erhardt, H. L. Falsetti, D. M. Davis, F. M. Abboud, P. B. McKay, and O. Y. Lim, "Spatial and temporal heterogeneity of left ventricular perfusion in awake dogs," vol. 94, pp. 748-754 1977.

- [61] P. Martirosian, U. Klose, I. Mader, and F. Schick, "FAIR True-FISP perfusion imaging of the kidneys," *Magn Reson Med*, vol. 51, pp. 353–361, 2004.
- [62] K. L. Miller, B. A. Hargreaves, J. Lee, D. Ress, R. C. deCharms, and J. M. Pauly, "Functional brainimaging using a blood oxygenation sensitive steady-state," *Magn Reson Med*, vol. 50, pp. 675-683, 2003.
- [63] E. Nagel, C. Klein, I. Paetsch, S. Hettwer, B. Schnackenburg, K. Wegscheider, and E. Fleck, "Magnetic resonance perfusion measurements for the noninvasive detection of coronary artery disease," *Circulation*, vol. 108, pp. 432–437, 2003.
- [64] K. S. Nayak, B. A. Hargreaves, B. S. Hu, D. G. Nishimura, J. M. Pauly, and C. H. Meyer, "Spiral balanced steady-state free precession cardiac imaging," *Magn Reson Med*, vol. 53, pp. 1468-1473, 2005.
- [65] K. S. Nayak, H. L. Lee, B. A. Hargreaves, and B. S. Hu, "Wideband SSFP: alternating repetition time balanced steady-state free precession with increased band spacing," *Magn Reson Med*, vol. 58, pp. 931-938, 2007.
- [66] R. Noeske, F. Seifert, K. H. Rhein, and H. Rinneberg, "Human cardiac imaging at 3 T using phased array coils," *Magn Reson Med*, vol. 44, pp. 978-982, 2000.
- [67] B. E. Northrup, K. S. McCommis, H. Zhang, S. Ray, P. K. Woodard, R. J. Gropler, and J. Zheng, "Resting myocardial perfusion quantification with CMR arterial spin labeling at 1.5 T and 3.0 T.," *J Cardiovasc Magn Reson.*, vol. 10, p. 53, 2008.
- [68] Y. Okada, K. Ohtomo, S. Kiryu, and Y. Sasaki, "Breath-hold T2-weighted MRI of hepatic tumors: value of echo planar imaging with diffusion-sensitizing gradient," *J Comput Assist Tomogr*, vol. 22, pp. 364–371, 1998.
- [69] R. J. Ordidge, M. Wylezinska, J. W. Hugg, E. Butterworth, and F. Franconi, "Frequency offset corrected inversion (FOCI) pulses for use in localized spectroscopy," *Magn Reson Med*, vol. 36, 1996.
- [70] W. R. Overall, S. M. Conolly, D. G. Nishimura, and B. S. Hu, "Oscillating dual-equilibrium steady-state angiography," *Magn Reson Med*, vol. 47, pp. 513-522, 2002.

- [71] J. R. Panning, P. D. Gatehouse, G. Z. Yang, F. Grothues, D. N. Firmin, P. Collins, and D. J. Pennell, "Abnormal subendocardial perfusion in cardiac syndrome X detected by cardiovascular magnetic resonance imaging.," *N Engl J Med* vol. 346, pp. 1948–1953, 2002.
- [72] J. Pauly, P. Le Roux, D. Nishimura, and A. Macovski, "Parameter relations for the Shinnar-Le Roux selective excitation pulse design algorithm," *IEEE Trans. Med. Imaging*, vol. 10, pp. 53 - 65 1991.
- [73] B. P. Poncelet, T. M. Koelling, C. J. Schmidt, K. K. Kwong, T. G. Reese, P. Ledden, H. L. Kantor, T. J. Brady, and R. M. Weisskoff, "Measurement of human myocardial perfusion by double-gated flow alternating inversion recovery EPI," *Magn Reson Med*, vol. 41, pp. 510-519, 1999.
- [74] J. G. Powles and "The Adiabatic Fast Passage Experiment in Magnetic Resonance " *Proc Phys Soc*, vol. 71, pp. 497 - 500, 1958.
- [75] E. D. Pracht, A. Fischer, J. F. T. Arnold, M. Kotas, M. Flentje, and P. M. Jakob, "Single-Shot Quantitative Perfusion Imaging of the Human Lung," *Magn Reson Med*, vol. 56, pp. 1347- 1351, 2006.
- [76] K. P. Pruessmann, M. Weiger, M. B. Scheidegger, and P. Boesiger, "SENSE: Sensitivity encoding for fast MRI.," *Magn Reson Med*, vol. 42, pp. 952–962, 1999.
- [77] P. M. Robson, A. J. Madhuranthakam, W. Dai, I. Pedrosa, N. M. Rofsky, and D. C. Alsop, "Strategies for reducing respiratory motion artifacts in renal perfusion imaging with arterial spin labeling," *Magn Reson Med*, vol. 61, pp. 1374-1387, 2009.
- [78] P. B. Roemer, W. A. Edelstein, C. E. Hayes, S. P. Souza, and O. M. Mueller, "The NMR phased array," *Magn Reson Med* vol. 16, pp. 192-225, 1990.
- [79] D. Rosenfeld and Y. Zur, "A new adiabatic inversion pulse," *Magn Reson Med*, vol. 36, pp. 124 - 136, 1996.
- [80] M. Schar, S. Kozerke, S. E. Fischer, and P. Boesiger, "Cardiac SSFP imaging at 3 Tesla," *Magn Reson Med*, vol. 51, pp. 799-806, 2004.
- [81] K. Scheffler and J. Hennig, "Is TrueFISP a gradient-echo or a spin-echo sequence?," *Magn Reson Med* vol. 49, pp. 395-397, 2003.

- [82] K. Scheffler and S. Lehnhardt, "Principles and applications of balanced SSFP technique," *European Radiology*, vol. 13, pp. 2409-2418, 2003.
- [83] P. Schmitt, M. A. Griswold, V. Gulani, A. Haase, M. Flentje, and P. M. Jakob, "A Simple Geometrical Description of the TrueFISP Ideal Transient and Steady-State Signal," *Magn Reson Med*, vol. 55, pp. 177-186 2006.
- [84] J. Schwitter, D. Nanz, S. Kneifel, K. Bertschinger, M. Büchi, P. R. Knüsel, B. Marincek, T. F. Lüscher, and G. K. von Schulthess, "Assessment of myocardial perfusion in coronary artery disease by magnetic resonance: a comparison with positron emission tomography and coronary angiography.," *Circulation*, vol. 103, pp. 2230-2235, 2001.
- [85] T. Shin, G. M. Pohost, and K. S. Nayak, "Systolic 3D First-Pass Myocardial Perfusion MRI: Comparison With Diastolic Imaging in Healthy Subjects," *Magn Reson Med*, vol. 63, pp. 858 - 864, 2010.
- [86] M. A. Sieber, P. Lengsfeld, J. Walter, H. Schirmer, T. Frenzel, F. Siegmund, H. J. Weinmann, and H. Pietsch, "Gadolinium-based contrast agents and their potential role in the pathogenesis of nephrogenic systemic fibrosis: the role of excess ligand.," *J Magn Reson Imaging*, vol. 27, pp. 955-962, 2008.
- [87] M. S. Silver, R. I. Joseph, and D. I. Hoult, "Highly selective $\pi/2$ and π pulse generation," *J Magn Reson*, vol. 59, pp. 327 - 351, 1984.
- [88] M. S. Silver and R. I. Joseph, "Selective spin inversion in nuclear magnetic resonance and coherent optics through an exact solution of the Bloch-Riccati equation," *Phys. Rev A*, vol. 31, pp. 2753-2755, 1985.
- [89] R. S. Staewen, A. J. Johnson, B. D. Ross, T. Parrish, M. H., and M. Garwood, "3-D FLASH imaging using a single surface coil and a new adiabatic pulse, BIR-4," *Invest Radiol*, vol. 25, pp. 559 - 567, 1990.
- [90] K. Sung and K. S. Nayak, "The design and use of tailored hard-pulse trains for uniform saturation of myocardium at 3 Tesla," vol. 60, pp. 997-1002, 2008.
- [91] K. Ugurbil, M. Garwood, and R. Bendall, "Amplitude and frequency modulated pulses to achieve 90° plane rotations with inhomogeneous B1 fields," *J Magn Reson*, vol. 72, pp. 177 - 185, 1987.
- [92] "United States Renal Data System," *USRDS 2009 annual data report, on-line*, 2009.

- [93] M. H. Vandsburger, R. L. Janiczek, Y. Xu, B. A. French, C. H. Meyer, C. M. Kramer, and F. H. Epstein, "Improved Arterial Spin Labeling After Myocardial Infarction in Mice Using Cardiac and Respiratory Gated Look-Locker Imaging With Fuzzy C-Means Clustering," *Magn Reson Med*, vol. 63, pp. 648–657 2010.
- [94] S. S. Vasanaawala, J. M. Pauly, and D. G. Nishimura, "Fluctuating equilibriumMRI," *Magn Reson Med*, vol. 42, pp. 876–883, 1999.
- [95] C. M. Wacker, F. Fidler, C. Dueren, S. Hirn, P. M. Jakob, G. Ertl, A. Haase, and W. R. Bauer, "Quantitative assessment of myocardial perfusion with a spin-labeling technique: preliminary results in patients with coronary artery disease," *J Magn Reson Imaging*, vol. 18, pp. 555–560, 2003.
- [96] A. Wagner, H. Mahrholdt, T. A. Holly, M. D. Elliott, M. Regenfus, M. Parker, F. J. Klocke, R. O. Bonow, R. J. Kim, and R. M. Judd, "Contrast-enhanced MRI and routine single photon emission computed tomography (SPECT) perfusion imaging for detection of subendocardial myocardial infarcts: an imaging study.," *Lancet*, vol. 361, pp. 374–379, 2003.
- [97] C. Waller, E. Kahler, K.-H. Hiller, K. Hu, M. Nahrendorf, S. Voll, A. Haase, G. Ertl, and Wolfgang R. Bauer, "Myocardial Perfusion and Intracapillary Blood Volume in Rats at Rest and with Coronary Dilatation: MR Imaging in Vivo with Use of a Spin-Labeling Technique," *Radiology* vol. 215, pp. 189–197, 2000.
- [98] D. J. J. Wang, X. Bi, B. B. Avants, T. Meng, S. Zuehlsdorff, and J. A. Detre, "Estimation of perfusion and arterial transit time in myocardium using free-breathing myocardial arterial spin labeling with navigator-echo," *Magn Reson Med*, vol. Early view, 2010.
- [99] E. C. Wong, R. B. Buxton, and L. R. Frank, "Quantitative imaging of perfusion using a single subtraction (QUIPSS and QUIPSS II)," *Magn Reson Med*, vol. 39, pp. 702 - 708, 1998.
- [100] E. C. Wong, M. Cronin, W. C. Wu, B. Inglis, L. R. Frank, and T. T. Liu, "Velocity-selective arterial spin labeling.," *Magn Reson Med*, vol. 55, pp. 1334-1341, 2006.
- [101] E. C. Wong, "Vessel-encoded arterial spin-labeling using pseudocontinuous tagging," *Magn Reson Med*, vol. 58, pp. 1086–1091, 2007.

- [102] W. C. Wu, E. r. Mohler, S. J. Ratcliffe, F. W. Wehrli, J. A. Detre, and T. F. Floyd, "Skeletal muscle microvascular flow in progressive peripheral artery disease: assessment with continuous arterial spin-labeling perfusion magnetic resonance imaging," *J Am Coll Cardiol*, vol. 53, pp. 2327 - 7, 2009.
- [103] F. Q. Ye, J. A. Frank, D. R. Weinberger, and A. C. McLaughlin, "Noise reduction in 3D perfusion imaging by attenuating the static signal in arterial spin tagging (ASSIST)." *Magn Reson Med*, vol. 44, pp. 92–100, 2000.
- [104] H. Zhang, M. Shea S, V. Park, D. Li, P. K. Woodard, R. J. Gropler, and J. Zheng, "Accurate myocardial T1 measurements: toward quantification of myocardial blood flow with arterial spin labeling," *Magn Reson Med*, vol. 53, pp. 1135–1142, 2005.
- [105] Z. Zun and K. S. Nayak, "Graphical derivation of the steady-state magnetization in balanced SSFP MRI," *In: Proceedings of the 14th Annual Meeting of ISMRM, Seattle*, p. 2410, 2006.
- [106] Z. Zun, E. C. Wong, and K. S. Nayak, "Arterial spin labeled myocardial perfusion imaging with background suppression," *In: Proceedings of the 16th Annual Meeting of ISMRM, Toronto*, p. 997, 2008.
- [107] Z. Zun, E. C. Wong, and K. S. Nayak, "Arterial Spin Labeled Myocardial Perfusion Imaging with Background Suppression: Initial Results," *In: Proceedings of the 11th Annual Meeting of SCMR, Los Angeles* p. 131, 2008.
- [108] Z. Zun, E. C. Wong, and K. S. Nayak, "Assessment of myocardial blood flow (MBF) in humans using arterial spin labeling (ASL): Feasibility and noise analysis.," *Magn Reson Med*, vol. 62, pp. 975-983, 2009.
- [109] Z. Zun, E. C. Wong, and K. S. Nayak, "Assessment of myocardial blood flow in humans using arterial spin labeling: Feasibility and noise analysis.," *In: Proceedings of the 17th Annual Meeting of ISMRM, Honolulu*, p. 1736, 2009.
- [110] Z. Zun, E. C. Wong, and K. S. Nayak, "Background Suppression Does Not Reduce Physiological Noise in Myocardial ASL Perfusion Imaging," *In: Proceedings of the 17th Annual Meeting of ISMRM, Honolulu*, p. 1735, 2009.
- [111] Z. Zun, E. C. Wong, and K. S. Nayak, "Myocardial ASL Perfusion Imaging Using Pulsed 2D Tagging of the Proximal Aorta," *In: Proceedings of the 17th Annual Meeting of ISMRM, Honolulu*, p. 1737, 2009.

- [112] Z. Zun, P. Varadarajan, R. G. Pai, E. C. Wong, and K. S. Nayak, "Arterial spin labeled MRI detects increase in myocardial blood flow with adenosine," *In: Proceedings of the 18th Annual Meeting of ISMRM, Stockholm*, p. 1309, 2010.
- [113] Z. Zun, P. Varadarajan, R. G. Pai, E. C. Wong, and K. S. Nayak, "Arterial spin labeled MRI detects increase in myocardial blood flow with adenosine," *In: Proceedings of the 13th Annual Meeting of SCMR, Phoenix*, p. 209, 2010.
- [114] Z. Zun, P. Varadarajan, R. G. Pai, E. C. Wong, and K. S. Nayak, "Arterial Spin Labeled MRI Detects Clinically Relevant Increases in Myocardial Blood Flow with Vasodilatation," *JACC Imaging*, in revision.
- [115] Y. Zur, S. Stokar, and P. Bendel, "An analysis of fast imaging sequences with steady-state transverse magnetization refocusing," *Magn Reson Med*, vol. 6, pp. 175–193, 1988.